POLITECNICO DI TORINO

Master's Degree in Aerospace Engineering

Master's Degree Thesis

Design of Identification and Compensation Methods for Space Rider GNC Algorithms

Supervisors
Prof. Elisa CAPELLO
Dr. Marco GIANNINI

Candidate
Cristiano GARINO

Academic Year 2021-2022

We demand rigidly defined areas of doubt and uncertainty!

Douglas Adams

Abstract

The ESA Space Rider System is designed to provide Europe with the first reusable and independent end-to-end orbital platform, to deliver an uncrewed orbital laboratory able to de-orbit, re-enter, land and be relaunched after limited refurbishment. In this context, AVIO is the prime contractor of the support module that must guarantee the guidance, navigation and control functions during the orbital phase of the system. High versatility and reliability are thus requested for the AVUM Orbital Module since the Space Rider mission foresees various in-orbit experiments, ranging from payload for commercial and institutional applications to In Orbit Verification/Demonstration missions, microgravity experiments, and Earth/Space observation. From this perspective, it becomes of paramount importance to manage all the operative conditions for which the GNC must guarantee the best performance in terms of accuracy and operative duration.

Attitude sensors must guarantee high data reliability despite being subjected to stresses during launch, a harsh operating environment and not least any assembly errors during integration. Constant in-orbit calibration is, therefore, necessary to meet requirements. Actuators, on the other hand, must be able to compensate for system and external uncertainties and manage any non-nominal condition. In particular, the malfunctioning or degraded behaviours of actuators are to be taken into account.

The objective of this thesis is to investigate the counteract action that the Space Rider's GNC must implement to identify and compensate for all the effects that could degrade the mission performance. Specifically, both sensor and actuator issues are addressed. To achieve this, sliding mode techniques are used for both identification and compensation phases, combined with closed-loop analysis of sensors and actuators. The performance and robustness of these algorithms are then demonstrated using simulations of real operating conditions that Space Rider will face in future missions.

Sommario

Il programma ESA Space Rider è stato progettato per fornire all'Europa la prima piattaforma orbitale end-to-end riutilizzabile e indipendente, al fine di fornire un laboratorio orbitale senza equipaggio in grado di de-orbitare, rientrare, atterrare ed essere rilanciato dopo una limitata revisione. In questo contesto, AVIO è il capo commessa del modulo di supporto che deve garantire le funzioni di guida, navigazione e controllo durante la fase orbitale del sistema. Per il modulo orbitale AVUM è richiesta un'elevata versatilità e affidabilità, poiché la missione Space Rider prevede diversi esperimenti in orbita, che vanno da payload per applicazioni commerciali ed istituzionali a missioni di verifica/dimostrazione in orbita, esperimenti in microgravità ed osservazione della Terra e dello spazio. Da questo punto di vista, diventa di fondamentale importanza la gestione di tutte le condizioni operative per le quali il GNC deve garantire le migliori prestazioni in termini di accuratezza e durata operativa.

I sensori di assetto devono garantire un'elevata affidabilità dei dati nonostante siano sottoposti a sollecitazioni durante il lancio, ad un ambiente operativo ostile e, non ultimo, ad eventuali errori di montaggio durante l'integrazione. Per soddisfare i requisiti è quindi necessaria una costante calibrazione in orbita. Gli attuatori, invece, devono essere in grado di compensare le incertezze di sistema e quelle esterne, e di gestire qualsiasi condizione non nominale. In particolare, è necessario trattare malfunzionamenti o comportamenti degradati dei singoli attuatori.

L'obiettivo di questa tesi è indagare le azioni di contrasto che il GNC di Space Rider deve attuare per identificare e compensare tutti gli effetti che potrebbero degradare le prestazioni della missione. In particolare, vengono affrontate le problematiche relative sia ai sensori che agli attuatori. A tal fine, vengono utilizzate tecniche basate sullo Sling Mode per entrambe le fasi di identificazione e compensazione, combinate con analisi in closed-loop di sensori e attuatori. Le prestazioni e la robustezza di questi algoritmi sono poi dimostrate tramite simulazioni di condizioni operative reali che Space Rider dovrà affrontare nelle missioni future.

Contents

List of Figures

List of Tables

Acronyms

ALEK	AVUM Life Extension Kit
AOM	AVUM Orbital Module
ARW	Angular Random Walk
AVUM	Attitude and Vernier Upper Module
ECI	Earth Centred Inertial
EKF	Extended Kalman Filter
ESA	European Space Agency
FTC	Fault tolerant Control
GNC	Guide, Navigation and Control
GPS	Global Position System
IXV	Intermediate eXperimental Vehicle
KF	Kalman Filter
IMU	Inertial Measurement Unit
LEO	Low Earth Orbit
LPS	Liquid Propulsion System
LVLH	Local Vertical local Horizontal
MED	Momentum Exchange Device
MEKF	Multiplicative Extended Kalman Filter
MPCB	Multi Purpose Cargo Bay
MTQ	MagneTorQuer
RAAN	Right Ascension of the Ascending Node
RACS	Roll Attitude Control System
RM	Re-entry Module
RWA	Reaction Wheel Assembly
SDAM	Solar Array Drive Mechanism
SMO	Sliding Mode Observer
SR	Space Rider
SRS	Space Rider System
STR	Star Tracker
VEGA	Vettore Europeo di Generazione Avanzata
VSS	Vega Space System
WRT	With Respect To

Chapter 1

Introduction

The history of space exploration only covers the last 70 years of human history. Nevertheless, it has made it possible to achieve enormous scientific breakthroughs, answer millennia-old questions and offer technical services to an increasingly interconnected population. With the unstoppable advances in technology, what seemed unattainable goals in the early missions of the 1960s became minimal goals in the following decades. As a result, there has been a trend toward designing missions with more and more stringent requirements.

The space environment offers conditions that cannot be found on Earth: it is possible to study the sky without being shielded by the atmosphere, experiments can be performed in microgravity, and Earth can be observed from a global perspective. But all this comes at a high cost, both in terms of risks, time, and money and in terms of technologies capable of withstanding this environment, which is as fascinating as it is hostile. Missions have thus demanded more autonomy and versatility on one hand and reliability on the other, to be able to cope with any off-nominal conditions without jeopardising the mission's success.

The Guidance, Navigation, and Control is one of the subsystems of greatest importance to ensure the success of a mission, allowing specifically to handle the attitude dynamics: communication from deep space, observation of distant galaxies or Earth remote sensing, require high pointing accuracies, which are provided both by the control itself and by the spacecraft attitude determination.

The work carried out in this thesis fits into this context, focusing on some issues concerning the GNC which might occur on Space Rider System, addressing specifically actuator degraded behaviours and attitude sensor misalignments.
Because of the types of missions that Space Rider will face, it is of paramount importance that the identification and compensation of such unforeseen conditions are carried out in orbit and in the shortest possible time.

Figure 1.1. Space Rider System render (credit: ESA [1])

Ground-based data analysis and instrument calibration/compensation are very costly for the mission; technical personnel needs a substantial amount of telemetry data to assess the problem, and the implementation and validation of correction algorithms is a time-consuming iterative process. Whether in missions scheduled to operate for several years this delay would affect only partially the final result, it would significantly reduce mission efficiency in the planned two months of orbital operations of the SR mission. In recent decades, these verification operations can be easily performed in orbit thanks to new techniques and improved processor performance.

On-orbit identification and compensation have several benefits, among which the most important are the minimisation of interruptions of science operations, a more precise pointing accuracy, a calibration more sensitive to thermal variations, optimised manoeuvres, and less ground support required. In addition, by decreasing the telemetry to be downloaded to the ground, the exchange of mission data can be significantly increased, which is particularly important for deep space missions. The timeliness of these topics is also proven by the direction in which the space market is going, which aims to have commercial software with real-time identification and compensation algorithms for problems that could arise in a space system.

Space Rider System has demanding pointing requirements regarding attitude determination (accuracy of 0.03°) and control (accuracy of 0.04°), which result in an overall required pointing accuracy of 0.05°. This work, carried out in cooperation with **AVIO**, arose from the necessity to guarantee the fulfilment of these requirements even under off-nominal conditions in which both actuators and attitude sensors might operate. Specifically, it will be addressed in-orbit Star Tracker misalignments and degraded cases that RWs might encounter. The main contribution brought by this thesis work concerns the robustness of the proposed methods, which do not merely identify problems but estimate their magnitude with non-linear estimators and propose dedicated compensations.

1.1 Literature review

Space-related systems are normally described with highly non-linear models where parameter uncertainty prevails. Over the years, different linearization techniques have been used to simplify models and, consequently, the algorithms used. However, linearized results often showed discrepancies with disturbances, unknown parameters, and parasitic dynamics. At the same time, non-linear mathematical approaches to determine and control states have arisen since the beginning of space missions, showing high potential but little application due to limited onboard processing capabilities. From the 1990s onward, the miniaturisation of electronics allowed for more performing processors in the space domain, enabling the in-orbit use of more robust algorithms. Among all, Sliding Mode techniques remain the most successful in handling disturbances and uncertainties in models [2].

The concept of Sliding surface introduced by Filippov [3] was initially primarily investigated in the Soviet literature [4]. Sliding modes come from the theory of Variable

Structure Systems, and in the space domain, they were first applied for robust control strategies. Subsequently, Sliding Mode Observer became widespread, allowing the estimation of states under unknown disturbances. Early on, to solve the inherent chattering problem of SM, the second-order sliding mode was explored, and the promising results led to the concept of higher-order sliding modes [5]. For the purposes of this thesis, mainly observers were investigated and tested, especially concerning the estimation of spacecraft attitude [6, 7, 8] and for the actuator fault identification [9, 10].

Despite their great potential, variable structures have not been used since the beginning of space missions. Since the second half of the 1950s, when interest arose in attitude determination, mathematical developments were very advanced compared to the applications in missions due to the limited onboard processing capabilities.
A distinction needs to be drawn between attitude determination and attitude estimation [11]: while the first one is a point-to-point approach, which does not make use of past measurements, the second refers to methods that use dynamic models of the system and past and current measurements to estimate attitude, and are therefore more computationally expensive.

The first algebraic method for the point-to-point attitude determination from a set of two observation vectors was developed by Harold Black in 1964, later renamed by Shuster the TRIAD method (Tri-Axial Attitude Determination System) [12]. Only one year later, Grace Wahba published her famous work [13] in which she posed the problem of attitude determination from any number of observation vectors. The first solutions to the problem were not applicable, and it had to wait until 1968 when Paul Davenport [14] proposed a practical algorithm, which solved the attitude problem for the quaternion parametrization, named the *q-method*. Due to the need to calculate eigenvalues and eigenvectors of a 4x4 matrix, it was unsuitable for 1970s onboard computers. The method finally found application thanks to the reformulation proposed by Shuster. In his QUaternion ESTimantion (QUEST), he avoided the eigenvalue/eigenvector decomposition, making the algorithm one of the most widely used in the years.

Even though some works on the topic were carried out earlier, the first paper on the Kalman Filter for attitude estimation was published by James Farrell [15]. It is a recursive algorithm which uses a series of measurements and system models, as well as noises, to estimate states with higher accuracy than a single measurement. The non-linearity of the spacecraft dynamics made it necessary to use an Extended Kalman Filter: despite being computationally more expensive, it is more robust to uncertainties than the point-to-point approach [16]. Literature works on the KF and its several versions (EKF, UKF, MEKF,...) are plenty, and the wide use made of it has been successful in many fields, including the one of sensor calibration [17]. Specifically, in this thesis, an EKF will be used to estimate misalignments of STRs in order to compare it with the results obtained with a SMO.

Due to the same limitations mentioned above, failure analysis in the space sector has only begun to be applied in recent decades. Simultaneously with the increase in onboard computing capabilities, performances required to GNC have increased, and requirements have become ever more demanding. Fault Tolerant Control must guarantee stability and performance properties even under failure. In order to be able to perform a wide range of experiments for a broad clientele, SRS has to be able to compensate for any failures in a timely manner, to make the most of the two months mission. An updated state-of-the-art review of FTC is presented by Amin [18]. The proposed method for identifying and compensating off-nominal cases of RWs of SRS is based on a SMO [19, 20] and on an adaptive FTC for optimal torque allocation [21].

1.2 Space Rider Program

The ESA Space Rider System is an uncrewed orbital platform able to de-orbit, re-enter, land and be relaunched after limited refurbishment. It will be the first European reusable and independent end-to-end space transportation system for Low Earth Orbit, which will transport payload for a large number of applications allowing technology demonstration and benefits research in pharmaceutics, biomedicine, biology and physical science.

SRS developed from the accumulated experience of *Intermediate eXperimental Vehicle* (figure 1.2). The IXV was the first European vehicle to perform an autonomous re-entry from LEO. The spaceplane lifted off at 13:40 GMT on 11 February 2015, from Europe's Spaceport in Kourou, French Guiana, in the 4th launch of the Vega rocket.

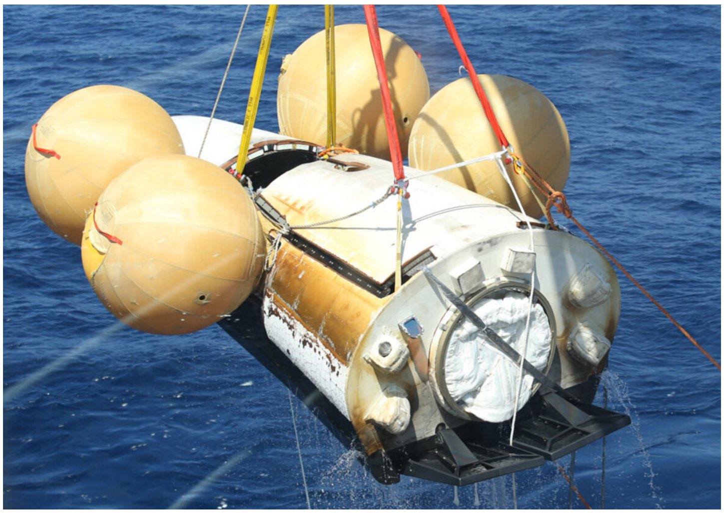

Figure 1.2. The IXV in the Pacific Ocean after a successful re-entry (credits: ESA [22])

Its suborbital flight reached an altitude of 412 km. The IXV registered an entry speed of 7.5 km/s at an altitude of 120 km, recreating the same conditions as those for a spacecraft returning from LEO. IXV decelerated gliding through the atmosphere it before deploying parachutes and then splashdown in the Pacific Ocean.
The IXV was a cornerstone mission, which opened the door to a wide range of possible manned or unmanned reusable missions from terrestrial orbits and beyond, which have to deal with hypersonic flight conditions.

Building on the success of the IXV program, ESA initiated a considerable effort to develop a reusable space transportation system to be integrated with the VEGA-C launcher, called precisely Space Rider System.
Once in operation, SRS will commercialise a novel service for various commercial and institutional space and non-space applications, performing a wide variety of experiments in microgravity, In-Orbit Demonstration/Validation missions for Earth observation, science and robotic exploration. The openable cargo bay will allow exposing payloads directly to open space or conversely will provide a pressurised environment if needed. The great potential lies in being able to transport the experiments back to Earth once the mission is complete.

Moving towards the end of operations on the International Space Station, this independent multipurpose orbital laboratory in LEO could become an inviting option for in-orbit experiments for customers worldwide.

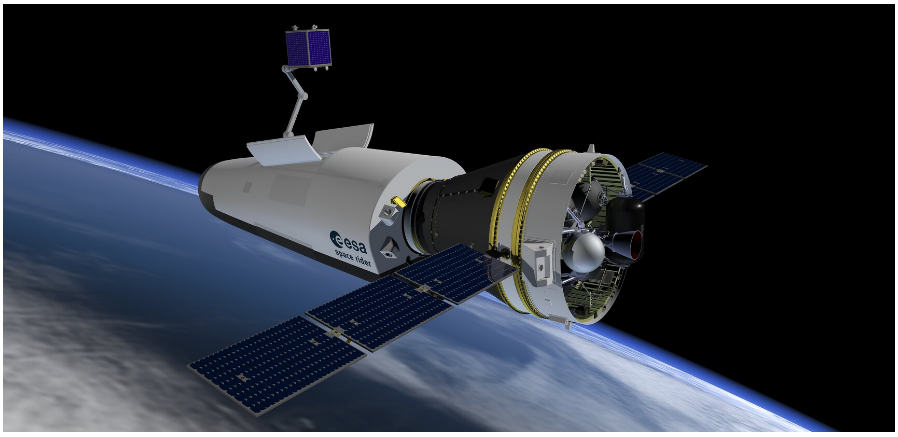

Figure 1.3. Space Rider System deploying a satellite (credit: ESA [1])

1.2.1 Space Rider System

The SRS is composed of two different modules, which have different functionalities, as well as different contractors.

SR-AOM The AVUM Orbital Module is a modified version of the Vega-C upper stage, and the prime contractor is AVIO. The AOM supplies power to the whole system, it handles telemetry data, proving as well thermal, attitude and orbit control. In this module are placed the propellant tanks. In fact, the module has a bi-propellant main propulsion (LPS) for the initial orbital injection and for de-orbiting, as well as a mono-propellant secondary propulsion (RACS) for roll and attitude control.
In order to guarantee an operational life of at least two months, AVUM has been equipped with the AVUM Life Extension Kit (ALEK), which accommodates the deployable solar panels, all the avionics and the attitude control systems. This module is part of a unified complete set of solutions and services for orbital exploitation and space transportation that AVIO is implementing to support the typical tasks of orbital platforms. They are all realised from modifications carried out to the AVUM stage, all of which fell within the Vega Space System (VSS) program. The AOM is

the expendable part of the SRS, and it is supposed to burn in the atmosphere.

SR-RM The Re-entry Module is the lifting body developed from accumulated experience on the IXV demonstrator. It is developed by Thales Alenia Space Italy, and it is equipped whit a Multi Payload Cargo Bay within which the experiments will return to Earth. Its design has been guided by maximising the volume of the cargo bay, which inside can be divided into numerous ways to accommodate payloads in different configurations. It has the ability to be pressurised as well as to expose payloads to the outside. The RM is the reusable part of the SRS and it is supposed to carry out at least 6 missions before being decommissioned.

Table 1.1 reports the most relevant data of the Space Rider.

Total length	$8.044m$
Launch mass	$4900kg$
Landing mass	$2850kg$
Power consumption	$600W$
Cargo bay volume	$1.2m^3$
Payload Mass	$620kg$
Flight time	$> 60days$
Number of missions	At least 6
Turnaround time	Under 6 months

Table 1.1. Space Rider specifications

Of particular interest for this work are the equipment used for attitude determination and control, specifically their function and operation. A list is therefore given here for completeness, while for the detailed descriptions and models used in the thesis, refer to chapter 2.

The AVUM is equipped with two STRs, one IMU (Accelerometer + Gyroscope) and a GPS receiver. In addition to the thrusters previously mentioned, there is a 4-wheels RWA and 3 magnetorquers.

The RM has recently taken on considerable importance for attitude determination in the orbital phase, as a third STR will be placed inside the MPCB.

1.2.2 Mission timeline

In a typical mission (figure 1.4), SRS will be launched from Kourou spaceport in French Guyana atop Vega-C. It will be injected in a 400km altitude orbit, and it is designed to operate at different orbital inclinations, from equatorial to SSO, depending on mission objectives. The platform will remain in a low-drag orbit for at least two months performing all scheduled scientific operations. At the end of operations, the SRS will execute a reentry boost to deorbit. After that, the Re-entry Module will separate from the AVUM Orbital Module and it will perform a ballistic coasting phase. Subsequently, RM will conduct an autonomous and controlled re-entry in the atmosphere, decelerating to a subsonic speed ($M < 0.8$). At this stage, at an altitude of about $16km$, a pilot chute, a conical ribbon drogue and a Disk-Gap-Band drogue are deployed in order to reach the desired condition to deploy a gliding parachute, called parafoil. From this point, the last phase of controlled descent begins, in which the parafoil will lead to a precise soft landing on the ground. The estimated landing accuracy is about 150m. Depending on orbital inclinations, the landing site may vary: for low inclination orbit and as well for the maiden flight, the landing site

Figure 1.4. Space Rider Reference Mission Timeline (credit: ESA [1])

will be Kourou (French Guyana), while Santa Maria (Azores) and Italy (site under consideration) are the sites considered for landings from orbits with inclinations $> 37°$.

In this way, payloads will be brought back to Earth. The landed RM will be then refurbished and integrated with a new AOM, to be ready to fly again. The estimated turnaround time is about 6 months.

Orbital phase

The orbital phase is the core of the mission and it is the part of the mission this thesis focused on. It starts a few seconds after reaching the target orbit, following the cut-off of circularization boost, allowing the starting of different AOM equipment (Avionics, Star Trackers initialization, Solar array deployment, etc.).

After the initial phase, a typical reference mission is the following:

- Four weeks in micro-gravity
- Two weeks for Space observation
- Two weeks for Earth observation

The micro-gravity phase is characterized by an attitude minimizing the control efforts and its baseline is Nose to Out of Plane orientation while ensuring the Sun following of the Solar arrays; when needed, also an MTQ-controlled attitude with nose towards Nadir is considered to reduce the induced vibration level.

The Space Observation is characterized by a Bay to Zenith orientation while ensuring Sun following of the solar arrays. A customer-defined orientation is an option.

The Earth Observation is characterized by a Bay to Nadir orientation while ensuring Sun following of the solar arrays. A variant can be a customer-defined orientation of the Bay wrt Nadir (tilt of the bay).

These main long phases can be interrupted by raising boosts, in case the altitude decay is deemed too high, or by Wait or Safe modes. The ground intervention during this orbital phase is permanent (provided the visibility from ground stations) to:

- Send the commands to the AOM and to the experiment if need
- Monitor the AOM status

Mission Status

At the present stage of the work, the maiden flight of the SRS is scheduled for the second half of 2024 at the earliest. The flight will be performed by VEGA-C as planned, which has meanwhile successfully executed its maiden launch on 13 July 2022 (figure 1.5).

Figure 1.5. Vega-C Maiden flight - liftoff (credit: ESA [23])

1.3 Thesis Outline

To summarise, the aim of this thesis is to provide robust identification and compensation methods to enhance the reliability of Space Rider GNC, applying them to both Star Tracker misalignments and off-nominal Reaction Wheel conditions. To ensure instantaneous handling of these conditions, Sliding Mode Observers are extensively used for the identification process. In the compensation phase, optimal conditions are sought.

- The chapter 1 has provided an introduction to the work carried out in the thesis, contextualising it in the scientific framework and relating it to the Space Rider mission. A description of the Space Rider System was also included.

- In chapter 2, all mathematical formulations and conventions are shown and explained. Reference frames, attitude parameterizations, dynamics and kinematic equations are reported, and sensor and actuator models are widely described.
- In chapter 3 is given a general introduction to the GNC subsystem, followed by a more detailed discussion of AOM GNC. It concludes with an explanation of off-nominal conditions from which the system might suffer.
- In chapter 4 are described the identification and compensation algorithms implemented in the simulator to handle off-nominal conditions.
- In chapter 5 are reported the results of simulations concerning the identification and compensation methods, applied to real mission scenarios. Moreover, conclusions and future works are discussed.

Chapter 2

Spacecraft mathematical model

This chapter contains models and mathematical formulations used in later chapters of the thesis. In particular, are reported reference systems used, attitude parameterizations and dynamics and kinematics equations, disturbance torques, and the SRS model with its actuators and sensors.

2.1 Reference frames

Depending on the mission type, different reference systems can be used in the attitude analysis. The following are those of most interest for this work.

2.1.1 Spacecraft Body Frame

A reference frame is always defined by the location of its origin and by the direction of its axes.

The body frame is the reference system used to determine the attitude of the spacecraft wrt another reference system, usually inertial. It is also the system wrt which positions and orientations of any equipment are provided. The Space Rider body frame has the origin in the centre of the intersection between the ALEK module and the RM, while its axes are oriented as follows. The X_B coincides with the symmetry axis of the

ALEK module pointing toward the RM, and it will also be aligned with the axial direction of VEGA-C. The Z_B axis is along the Solar Arrays axes, and the Y_B axis is orthogonal to the other two to complete the direct triad, and moreover, it also points in the direction of the cargo bay.

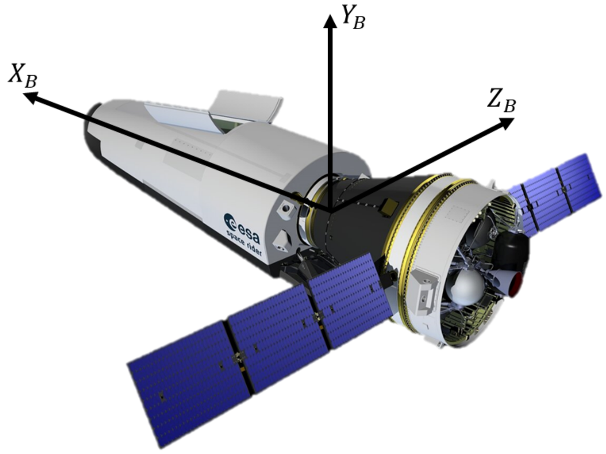

Figure 2.1. Space Rider Body reference frame

2.1.2 Earth-Centered Inertial Frame

The ECI system will be used as an inertial system wrt which the orientation of the body system will be verified. Even if the frame isn't exactly inertial due to the Earth's rotation around the Sun, will be considered inertial with no appreciable error for LEO dynamics.

The ECI is centred in the centre of the Earth, considered spherical. The X_{ECI} axis lays in the equatorial plane and points toward the vernal equinox, the Z_{ECI} axis points toward the North pole and the Y_{ECI} axis lays in the equatorial plane is orthogonal to the other two in order to complete the direct triad.

2.1.3 Local-Vertical Local-Horizontal Frame

The LVLH frame is also often used to describe the spacecraft's attitude, for its ease of viewing along the orbit, or the relative motion of between orbiting bodies.

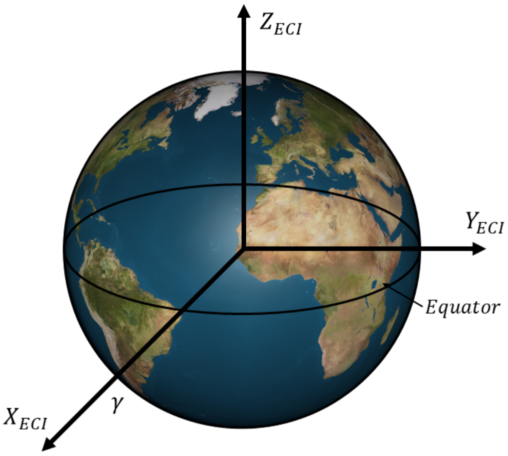

Figure 2.2. ECI reference frame

LVLH frame is centred in the centre of mass of the spacecraft. The X_{LVLH} axis is directed along the vertical direction, pointing in the opposite direction to the Earth, the Z_{LVLH} axis is in the direction of the kinetic moment, defined as the cross-product of the position and the velocity of the spacecraft, and the Y_{LVLH} axis is orthogonal to the other two in order to complete the direct triad.

The LVLH reference frame moves along the orbit with the spacecraft, is a rotating frame, and then it's non-inertial.

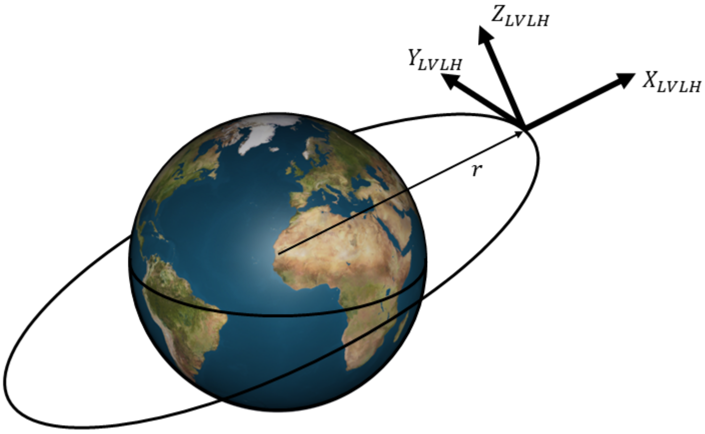

Figure 2.3. LVLH reference frame

2.2 Attitude Parameterizations

In spacecraft motion, the attitude indicates the rotation between the spacecraft reference frame and a reference frame. The attitude motion is described by the attitude dynamics equation, to determine the variations of the angular velocity, and by the kinematic equation to relate the attitude parameters to the angular velocity. Attitude can be parameterized in several ways: Euler's angles, directional cosine matrix, Rodrigues parameters, quaternions and many others. For the purpose of this thesis, it will be used and therefore described Euler angles and quaternions.

2.2.1 Euler's Angles

Attitude can be fully defined using three parameters, and the most widely used set of three parameters which describes the attitude of a rigid body (or identically the attitude of a body frame) with respect to a fixed frame are the Euler's angles. It is in fact possible to rotate the fixed frame onto any arbitrary frame using three consecutive rotations about different axes, and the angle of each rotation is called Euler's angle. By convention, let's call the first angle ϕ, the second one θ and the third ψ. Each rotation about the relative axes can be described with an elementary rotation matrix, and then the transformation matrix L_{BI}[1] is a function of the three angles which simple matrix operations can determine.

As an example, a widely used sequence of rotation in space flight dynamics and also in flight mechanics is the $3-2-1$ rotation, also known as the *Tait-Bryan*, whose rotation matrix is

$$L_{BI} = R_3(\phi)R_2(\theta)R_1(\psi) \tag{2.1}$$

where

$$R_3(\phi) = \begin{bmatrix} 1 & 0 & 0 \\ 0 & \cos(\phi) & \sin(\phi) \\ 0 & -\sin(\phi) & \cos(\phi) \end{bmatrix} \tag{2.2}$$

---

[1] By convention, L_{BI} indicates the rotation from the fixed frame I to the body frame B

$$R_2(\theta) = \begin{bmatrix} \cos(\theta) & 0 & -\sin(\theta) \\ 0 & 1 & 0 \\ \sin(\theta) & 0 & \cos(\theta) \end{bmatrix} \tag{2.3}$$

$$R_1(\psi) = \begin{bmatrix} \cos(\psi) & \sin(\psi) & 0 \\ -\sin(\psi) & \cos(\psi) & 0 \\ 0 & 0 & 1 \end{bmatrix} \tag{2.4}$$

Euler's angles are not uniquely defined, and it is possible to move from one reference system to another by performing different rotations around different axes, and given a set of Euler angles, these are not commutative. Furthermore, by describing rotations in three-dimensional space with three parameters, one may incur singularities, i.e. when the Euler's angles are not uniquely defined to define the relative position of the two reference systems in which the rotation sequence is chosen. For *Tait-Bryan*'s angles the singularity occurs for $\cos(\theta) = 0$ or $\theta = \pi/2 \pm k\pi$.

2.2.2 Quaternions

W. R. Hamilton introduced quaternions in 1843 [24], and they are a number system extending the complex numbers. They are useful for expressing attitudes and rotations, avoiding singularities, and reducing computational costs. Compared to Euler's angles, where three consecutive rotations around three axes define the coordinate change, quaternions use a unique rotation α around a single axis $\boldsymbol{a}$, that is fixed in both frames to define the coordinate change completely.

According to the Euler axis-angle representation, they are composed of four components

$$\mathbf{q} = q_0 + \boldsymbol{q_v} = q_0 + q_1\hat{\boldsymbol{i}} + q_2\hat{\boldsymbol{j}} + q_3\hat{\boldsymbol{k}} \tag{2.5}$$

where q_0 is the scalar component and $\boldsymbol{q_v}$ is the vector part of the quaternion, which express the magnitude of the rotation and the axis of rotation respectively, and they are related to α and $\boldsymbol{a}$ by:

$$q_0 = \cos\left(\frac{\alpha}{2}\right)$$
$$q_1 = a_1 \sin\left(\frac{\alpha}{2}\right)$$

$$q_2 = a_2 \sin\left(\frac{\alpha}{2}\right)$$
$$q_3 = a_3 \sin\left(\frac{\alpha}{2}\right)$$

The four quaternion components are related by the equation below, which guarantees that the quaternion is unitary:

$$||\boldsymbol{q}|| = \sqrt{q_0^2 + q_1^2 + q_2^2 + q_3^2} = 1$$

For the purpose of this thesis, let's recall the conjugate of a quaternion, which is defined in the following way

$$\mathbf{q*} = q_0 - q_1\hat{\boldsymbol{i}} - q_2\hat{\boldsymbol{j}} - q_3\hat{\boldsymbol{k}} \tag{2.6}$$

and the inverse quaternion:

$$\boldsymbol{q^{-1}} = \frac{\boldsymbol{q*}}{||\boldsymbol{q}||^2} \tag{2.7}$$

Let's define the quaternion product as

$$\boldsymbol{q} \otimes \boldsymbol{q'} = \Omega(\boldsymbol{q})\boldsymbol{q'} = \Psi(\boldsymbol{q'})\boldsymbol{q} \tag{2.8}$$

where

$$\begin{aligned} \Omega(\boldsymbol{q}) &= \begin{bmatrix} q_0 & -\boldsymbol{q_v}^T \\ \boldsymbol{q_v} & q_0\mathbb{1}_3 + [\boldsymbol{q_v}\times] \end{bmatrix} \\ \Psi(\boldsymbol{q'}) &= \begin{bmatrix} q_0' & -\boldsymbol{q_v'}^T \\ \boldsymbol{q_v'} & q_0'I_3 - [\boldsymbol{q_v'}\times] \end{bmatrix} \end{aligned} \tag{2.9}$$

and I_3 is the identity matrix of dimension 3 and $[\boldsymbol{q}\times]$ is the skew-symmetric matrix defined as:

$$[\boldsymbol{q}\times] = \begin{bmatrix} 0 & -q_3 & q_2 \\ q_3 & 0 & -q_1 \\ -q_2 & q_1 & 0 \end{bmatrix} \tag{2.10}$$

It is important to remember that the quaternion product is not commutative, but possesses distributive and associative properties.

A benefit of quaternions in calculations compared to Euler's angles is that successive rotations can be represented using quaternion multiplications. For the sake of completeness, the rotation matrix is therefore expressed using the quaternion formulation:

$$L_{BI} = (|q_0|^2 - ||\boldsymbol{q_v}||^2)\mathbb{1}_3 + 2\boldsymbol{q_v}\boldsymbol{q_v}^T + 2q_0[\boldsymbol{q_v}\times] \tag{2.11}$$

The main drawback of quaternions is given by their difficult visualisation, and for this reason, Euler's angles will be used instead to graphically express rotations and attitudes. The conversion between the two formulations is obtained through the following relation:

$$\begin{bmatrix} \phi \\ \\ \theta \\ \\ \psi \end{bmatrix} = \begin{bmatrix} \arctan\left(\dfrac{2(q_0q_1 + q_2q_3)}{1 - 2(q_1^2 + q_2^2)}\right) \\ \arcsin(2(q_0q_2 - q_3q_1) \\ \arctan\left(\dfrac{2(q_0q_3 + q_1q_2)}{1 - 2(q_2^2 + q_3^2}\right) \end{bmatrix} \tag{2.12}$$

2.3 Attitude Kinematics

The attitude kinematics represents the evolution of the spacecraft's attitude parameters, relating them to the angular velocity. Hereafter are reported equations using both Euler's angles and quaternions, as both will be used in the continuation of the thesis.

The differential equations with Euler's angles parameterization have the following form

$$\begin{Bmatrix} \dot{\phi} \\ \dot{\theta} \\ \dot{\psi} \end{Bmatrix} = \begin{bmatrix} \cos(\psi)\cos(\theta) & \sin(\psi) & 0 \\ -\sin(\psi)\cos(\theta) & \cos(\psi) & 0 \\ \sin(\theta) & 0 & 1 \end{bmatrix} \begin{Bmatrix} \omega_1 \\ \omega_2 \\ \omega_3 \end{Bmatrix} \tag{2.13}$$

where $\boldsymbol{\omega}_B = [\omega_1, \omega_2, \omega_3]^T$ is the spacecraft angular velocity computed in the body reference frame.

Using quaternions, the differential equations assume instead the following structure

$$
\begin{aligned}
\begin{Bmatrix} \dot{q}_0 \\ \dot{q}_1 \\ \dot{q}_2 \\ \dot{q}_3 \end{Bmatrix} &= \frac{1}{2} \begin{bmatrix} q_0 & -q_1 & -q_2 & -q_3 \\ q_1 & q_0 & -q_3 & q_2 \\ q_2 & q_3 & q_0 & -q_1 \\ q_3 & -q_2 & q_1 & q_0 \end{bmatrix} \begin{Bmatrix} 0 \\ \omega_1 \\ \omega_2 \\ \omega_3 \end{Bmatrix} \\
&= \frac{1}{2} \begin{bmatrix} 0 & -\omega_1 & -\omega_2 & -\omega_3 \\ \omega_1 & 0 & \omega_3 & -\omega_2 \\ \omega_2 & -\omega_3 & 0 & \omega_1 \\ \omega_3 & \omega_2 & -\omega_1 & 0 \end{bmatrix} \begin{Bmatrix} q_0 \\ q_1 \\ q_2 \\ q_3 \end{Bmatrix}
\end{aligned} \tag{2.14}
$$

which in the commonly used form has the following compact notation :

$$\dot{\boldsymbol{q}}(t) = \frac{1}{2}\Omega(\boldsymbol{\omega}_B(t))\boldsymbol{q}(t) \tag{2.15}$$

2.4 Attitude Dynamics

To obtain an explicit formulation of the angular velocity variation, we can use the second law of rigid body which states that the derivative of the angular momentum is equal to the total external torque applied to the body itself. Let's define the total angular momentum as the sum of the spacecraft angular momentum and the angular momentum of the Momentum Exchange Devices

$$\boldsymbol{H}_{tot} = \boldsymbol{H}_{s/c} + \boldsymbol{H}_{med} \tag{2.16}$$

and then the law can be expressed as follows:

$$\dot{\boldsymbol{H}}_{tot} = \dot{\boldsymbol{H}}_{s/c} + \dot{\boldsymbol{H}}_{med} = \boldsymbol{T}_{ext} \tag{2.17}$$

Where $\boldsymbol{T}_{ext}$ is the external torque, including both external disturbances and actuators producing external torques. By expressing each term in the body reference frame and considering a constant inertia matrix J, the equation becomes:

$$J\dot{\boldsymbol{\omega}}_B + \boldsymbol{\omega}_B \times J\boldsymbol{\omega}_B + \dot{\boldsymbol{H}}_{med} + \boldsymbol{\omega}_B \times \boldsymbol{H}_{med} = \boldsymbol{T}_{ext} \tag{2.18}$$

Where $\dot{\boldsymbol{H}}_{med} = -\boldsymbol{T}_{med}$ is the torque of the MED, being equivalent to the negative torque in the body frame. The Euler's equation is then obtained in the following form:

$$\dot{\boldsymbol{\omega}}_B = -J^{-1}(\boldsymbol{\omega}_B \times (J\boldsymbol{\omega}_B + \boldsymbol{H}_{med}) + \boldsymbol{T}_{med} - \boldsymbol{T}_{ext}) \tag{2.19}$$

2.5 Disturbance Torques

As described in section 2.4, to correctly predict the attitude, it's required to have a model of the disturbance torque, which is likely simulating their magnitudes in the different phases of the mission. For this reason, are now provided models describing gravity gradient torque, aerodynamic torque, magnetic dipole torque and solar radiation torque.

2.5.1 Gravity Gradient Torque

A non-symmetrical spacecraft in a gravity field is subjected to a gravity-gradient torque. This torque arises due to the different intensities of the gravity force to which different spacecraft parts are subjected, especially when it is large enough.

Assuming a spherical mass distribution for the planet, Earth in this case, it can be derived the gravity gradient torque for a continuous body by calculating in first instance the infinitesimal force $d\boldsymbol{F}$ felt by each dm of the spacecraft, and then calculating the total torque by integrating the product between $d\boldsymbol{F}$ and the position $\boldsymbol{r}$ of the infinitesimal mass relative to the spacecraft geometric centre. Hereafter, the final expression of the gravity gradient torque

$$\boldsymbol{T}_{gg} = \frac{3\mu}{\boldsymbol{R}_b^3}[\boldsymbol{R}_b \times (\boldsymbol{J}\boldsymbol{R}_b)] \tag{2.20}$$

where $\mu = GM_{\oplus} = 3.986 \cdot 10^{14} m^3/s^2$ is the Earth's gravitational constant, $\boldsymbol{J}$ is the inertia matrix and $\boldsymbol{R}_b$ is the position of the spacecraft geometric centre wrt the centre of the Earth.

Simplified formulations can be obtained in the case of a diagonal $\boldsymbol{J}$ matrix, but in the case of SRS, these simplifications cannot be made.

2.5.2 Aerodynamic Torque

A spacecraft orbiting around Earth in LEO is affected by its upper atmosphere. The atmospheric drag is low, but not zero, and the resulting torque is dominant for spacecrafts in LEO. At this height, the continuous model is no more effective due to low density, and so the drag effects on the spacecraft are treated at the molecular level. Numerous models accurately describe the atmosphere above $120km$, which include solar and geomagnetic activity and diurnal and orbital variations. Based on their data, the following density variation model has been implemented, taking into account the sinusoidal nature of the atmospheric density along the orbit's path:

$$\rho(t) = \rho_0 + \Delta\rho\left(\frac{2\pi t}{T} + \theta_0\right) \tag{2.21}$$

Where ρ_0 is the mean atmospheric density, $\Delta\rho$ the respective variation, T the orbital period, and θ_0 a configurable offset. The proposed function is thus dependent on atmospheric conditions, orbital elements, solar activity and epoch.

The force produced on a surface element dA with outward normal vector $\boldsymbol{N}$ is the following:

$$d\boldsymbol{F}_D = -\frac{1}{2}C_D\rho V^2(\boldsymbol{N}\cdot\boldsymbol{V})\boldsymbol{V}dA \tag{2.22}$$

where $\boldsymbol{V}$ is the unit vector in the direction of the translational velocity V of the surface element wrt the incident stream. The parameter C_D is the drag coefficient. Note that the drag coefficient is a parameter that depends not only on the surface structure but also on the local angle-of-attack and thus, fixing a numeric value for C_D is only an approximation.

The aerodynamic torque acting on the spacecraft due to the force over the surface is

$$\boldsymbol{T}_D = \int \boldsymbol{r}\times d\boldsymbol{F}_D dA \tag{2.23}$$

where $\boldsymbol{r}$ is the vector from the spacecraft centre-of-mass to the surface element dA.

There are numerous simplified models, but given the magnitude of this disturbance, a more precise calculation is required for accurate simulation results.

2.5.3 Magnetic Dipole Torque

Magnetic dipole torque results from the interaction between an external magnetic field and the spacecraft's residual magnetic dipole. Hysteresis and spacecraft magnetic moments are the primary sources of this torque. This torque can be expressed as

$$\boldsymbol{T}_{mag} = \boldsymbol{M} \times \boldsymbol{B} \tag{2.24}$$

where $\boldsymbol{M}$ is the sum of the residual dipoles of the spacecraft and $\boldsymbol{B}$ is the external magnetic field, in this instance, the Earth. Spacecraft residual moment is strongly dependent on the onboard equipment and materials, while in the case of Earth's magnetic field, it can be calculated as a function of the distance between the centre of Earth and the spacecraft R. Let's call $M = 7.96 \cdot 10^{1}5 kg/m$ the Earth magnetic constant. The module of the Earth's magnetic field is then

$$B = \frac{M\lambda}{R^3} \tag{2.25}$$

where λ is a unit-less parameter function of the latitude, ranging from 1 at the magnetic equator to 2 at the magnetic poles.

2.5.4 Solar Radiation Torque

Solar radiation incident on a spacecraft produces a force in its centre of pressure, which causes a torque when the centre of pressure does not coincide with the centre of mass. Since sunlight consists of particles with mass, it has a momentum that generates pressure once it hits a surface, which is called radiation pressure: it is a function of the distance from the Sun, and it can be easily obtained as

$$p = \frac{I_s}{c} \tag{2.26}$$

where I_s is the solar constant[2] which is equal to $1366 W/m^2$ at $1 AU$[3], and $c = 3 \cdot 10^8 m/s$ is the speed of light. It is straightforward to obtain that in LEO $p = 4.55 \cdot 10^{-6} N/m^2$.

---

[2] The solar constant is a flux density measuring mean solar electromagnetic radiation per unit area

[3] An Astronomical Unit is a length unit that indicates the mean distance between Earth and Sun

The most commonly used simplified model to describe solar radiation torque is given by:

$$T_{solar} = p(1+f)A_s \cos(\phi)(c_{pa} - c_g) \tag{2.27}$$

Where the new terms are A_s, the effective sunlit spacecraft area, ϕ, the solar incidence angle, the reflectance factor f, ranging from 0 (total absorption) to 1 (total reflection) and the distance between the centre of pressure c_{pa} and the centre of mass c_g.

2.6 Sensor models

SRS has installed dozens of sensors to monitor the very health of the system. The sensors of interest for the purpose of this work are those related to the determination of attitude parameters, i.e. the STRs and gyroscopes.

2.6.1 Star tracker model

SRS is equipped with 3 Star Tracker SPACESTAR of Leonardo. SPACESTAR is an innovative star tracker architecture, which differs from the state-of-the-art architectures with software running directly on the onboard computer of the ADCS. In this way, SPACESTAR hardware is composed of Optical Heads (up to three per satellite), each hosting the optics, the detector and some simple digital electronics to guarantee communications with the ADCS computer. The design of the Optical Head of SPACESATR is based on Leonardo's space-qualified AA_STR star tracker. This platform enables an essential reduction in power consumption, mass and size, and combined with the software is able to extrapolate the quaternion solution starting from compressed sky images, without the necessity of converters or other unnecessary hardware. During operations, the onboard computer runs the SPACESTAR[4] software with a frequency of $10Hz$.

This sensor provides very precise, but not error-free measurements. In order to obtain an accurate measurement model, the following error sources are implemented

---

[4] *Satellite Platform Avionics Computer Embedding Star Tracker Algorithms And Resources*

in the simulator; they refer to a single SPACESTAR's optical head and they are expressed in the single head boresight reference frame:

- Bias errors are considered as all the error sources affecting the knowledge of the STR measurement frame wrt an external spacecraft reference frame. Table 2.1 reports error sources and errors and numerical values.
- Low-frequency errors are reported in table 2.2 and are referred to a typical mission of 15 years.
- Random errors include the frequency of spatial contributions and temporal noise. These errors are angular velocity dependent and are reported in table 2.3.

Error Source	Error (3σ) [$arcsec$]	
	Pitch/Yaw	Roll
Misalignment measurement R_A[5] to R_{meas}[6]	13	33
Misalignment between R_A and R_{meas} after STR delivery	3	3
Ground to orbit boresight stability	5	2
Overall	15	35

Table 2.1. Bias Error

Error Source	Error (3σ) [$arcsec$]	
	Pitch/Yaw	Roll
Relativistic aberration ($0.1Km/sec$)	0.07	0.67
Star catalogue error ($\pm 7.5year$)	0.5	4
Residual in flight focal length calibration ($3\mu m$)	1	1
Optical distorsion	1.3	2.6
Residual focal length chromatic distortion	1	2
Boresight Stability [$DT = \pm 10°C$]	1.5	0.3
Overall	2.49	5.31

Table 2.2. Low frequency Error

---

[5] Optical cube reference frame

[6] Star Tracker measurement (boresight) reference frame

S/C Rate [deg/sec]	Error (3σ) [$arcsec$]	
	Pitch/Yaw	Roll
0.1	9.5	75
0.5	12	94.5
1.0	20	150
2.0	40	300

Table 2.3. Overall Random Error

The 3 SPACESTAR STR are placed respectively two on the AOM and one inside the MPCB of the RM, close to payloads. When they are pointing towards the sky, they can measure attitude, but when they are pointing at the Earth, the Moon or when they are exposed to the sunlight they are in a blinding condition. For this reason, it is necessary to have multiple STRs to ensure a more continuous data acquisition.

The installation of the third STR in the cargo bay became necessary during the design phase, in order to obtain more accurate attitude data coming from a sensor located close to the payload, and therefore less subject to the uncertainties induced by the structure between the MPCB and the STR on the AOM. In fact, STRs on the AOM, being some meters far from the bay, give measurements prone to errors due to thermo-elastic deformations, misalignments induced by flight vibrations, and possible assembly errors. These possible incorrect orientation could result in measurements that are not compliant with the imposed requirements. For the above-mentioned reasons, in addition to providing data under nominal operating conditions, this STR will be used to calibrate the two STRs on the AOM in orbit.

Defining the X_{STR} axis of STR reference frame aligned with the boresight, and the Y_{STR} and Z_{STR} axes lying in the perpendicular plane to complete the right triad, we can define the orientation of the STRs on the AOM (figure 2.4) wrt the body reference frame, expressed with 321-Euler's angles parameterization:

$$\alpha_{STR1} = [150^\circ,\ 30^\circ,\ 0^\circ]^T \tag{2.28}$$

$$\alpha_{STR2} = [210^\circ,\ 30^\circ,\ 0^\circ]^T \tag{2.29}$$

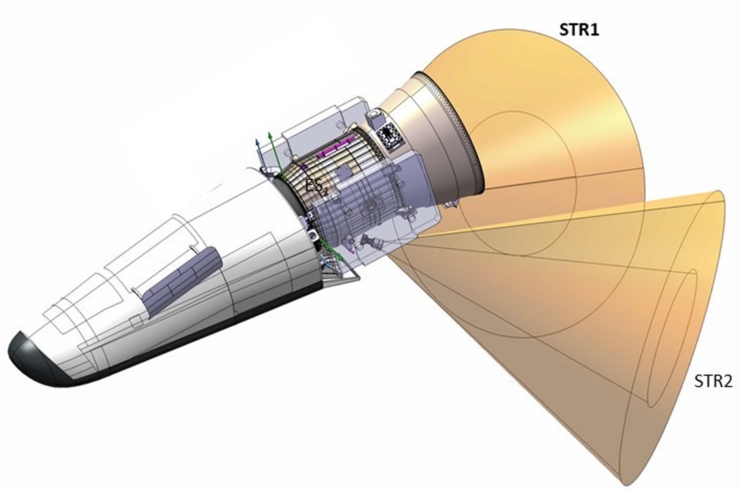

Figure 2.4. AVUM's Star Trackers

The third STR, mounted in the MPCB, will have an orientation that has not yet been definitively decided but it will certainly be inclined wrt the nadir direction to be able to intercept a portion of the sky between the bay structure and the Earth. For now, the orientation wrt the body reference frame is assumed to be:

$$\alpha_{STR_{REF}} = [75°,\ 30°,\ 30°]^T \tag{2.30}$$

2.6.2 Gyroscope model

Gyroscopes are integrated inside the Inertial Measurement Unit, as well as the accelerometer. It is the sensor used to measure the angular velocity of the spacecraft wrt inertial space. To completely define the angular velocity of SRS, at least 3 gyros are required.
Being composed of several mechanical parts, the measurement is modelled taking into account the effects coming from multiple causes. A general mathematical formulation for the gyro output measurement is [25]:

$$\omega_{meas} = (1 + k)\omega_{true} + b + \eta \tag{2.31}$$

where k is a small correction to the nominal scale factor, b represents the drift rate and η is the noise on the gyro output (ARW). This formulation can be expanded by detailing the contributions:

- The Angular Random Walk noise models the average error occurring when the signal is integrated for the angle computation. The longer the signal is integrated, the more the error will increase and it provides a fundamental limitation to any angle measurement that relies solely on the integration of rate. It arises from high-frequencies noise, such as electrical noises and so on.
  The ARW can be modelled as an additive Gaussian white noise using the following standard deviation
  $$\sigma_{ARW} = ARW\sqrt{B} \tag{2.32}$$
  where B is the bandwidth and ARW is a coefficient which is provided by the supplier.

- The bias instability is normally modelled as a first-order Gauss-Markov process and it models how the bias of the sensor changes over a specified period of time at a constant temperature (i.e. low-frequency drift). The variance of the bias instability can be estimated by means of the Allan Variance technique, and it can be modelled as:
  $$\dot{b}(t) = -\beta b(t) + \eta_c \tag{2.33}$$
  where β is the inverse of the correlation time T_c and η_c is Gaussian white noise with covariance σ_{η_c}

2.7 Actuator models

AVUM has different actuators for orbital and attitude control. While the LPS is used for orbital manoeuvres, reaction wheels, magnetorquers and RACS are the ones for attitude control. For the purpose of this thesis, only attitude actuators are discussed, and also RACS are neglected as not being part of the work carried out.

2.7.1 Reaction wheels

A reaction wheel is the most widely used actuator for attitude control. RW is a Momentum Exchange Device, in which an electric motor put a wheel in rotation, and when the wheel's speed is changed a torque is produced, and for the conservation of the angular momentum, an equal and opposite torque is applied to the spacecraft. In this way, RW allows for reaching higher accuracies in the control. They are classified by the torque provided and the quantity of angular momentum stored. To ensure 3-axis control, 4 RWs are normally used. Although in past missions numerous RWs operated nominally for decades, others suffered failures which had big impacts on several missions. Due to this, the fourth extra RW is nowadays a common choice. The RWs can be organised into different geometric configurations, which are usually called assemblies.

Regardless of the chosen RWA, the behaviour of an individual RW can be described and then modelled by taking into account several considerations.

- **Saturation** The RW suffers two different saturations, one on the maximum acceleration of the wheel which limits the maximum torque provided, and the other one on the maximum speed of the wheel which limits the maximum angular momentum stored. If the RW is subject to this second saturation, it can only provide torque that moves the wheel away from saturation, i.e. only negative torque can be applied when saturation reaches the upper bound, and only positive torque when the wheel is negatively saturated.

- **Friction effects** Following the LuGre model [26], different sources of friction are taken into account: static, Coulomb and viscous. Static friction (stiction), also known as break-away friction, corresponds to the minimum force to be done to begin the movement. The Coulomb effect is the minimum amount of friction between two lubricated surfaces in relative motion, which is independent of the magnitude of the velocity. The viscous effect is velocity-dependent friction that corresponds to a scale factor in produced torque wrt the angular speed of the wheel caused by the increase in the lubricant viscosity as the wheel speed increases. The union of the preceding effects produces a further effect called the Stribeck effect, which consists of transition zones in which friction decreases with the increase of the relative speed.

$$T_f = \underbrace{T_b \omega_w}_{\text{Viscous friction}} + \underbrace{T_c sign(\omega_w)}_{\text{Coulomb friction}} + \underbrace{(T_s - T_c)\exp\left[-\left(\omega_w/\omega_s\right)^2\right] sign(\omega_w)}_{\text{Break-away friction + Stribeck effect}} \tag{2.34}$$

where T_f corresponds to the torque generated due to friction, T_b is the viscous friction coefficient, T_c is the Coulomb friction coefficient, T_s is the stiction coefficient, ω_w is the wheel angular speed and ω_s is the Stribeck angular velocity.

- **Wheel imbalances** This effect presents its greatest effects in high frequencies. To take this into account in RW model, whose characteristic frequency would not allow such phenomena to be appreciated, is represented using a white noise signal with equivalent energy to the real phenomena, but at a reduced frequency of $5HZ$.
- **Tachometer** A RW is provided with a tachometer, which can be digital or analogical, and it's used to detect the wheel's rotational speed. The result is a quantified measure of the ω_{RW}

Table 2.4 shows the numerical values of the parameters of the RW employed by SR, which are provided by the supplier.

T_{max}	0.22 Nm
H_{max}	45 Nms
I_{RW}	0.107 kgm^2
T_b	5e-5 Nm
T_c	2.5e-3 Nm
T_s	0.006 Nm
ω_s	0.01 rad/s

Table 2.4. Reaction Wheel parameters

SRS uses a 4-Wheel Symmetric Pyramid configuration, and each RW is mounted according to two different angles, the aperture angle α and the clocking angle β. Figure 2.5 reports a schematic representation of the configuration and conventions adopted, in which the direction of rotation of the RW is consistent with the z_{RW} of the RW local frame. By recalling the convection used for the X_B, it is evident that the RWA, positioned in the AOM, is mounted around the symmetry axis of the module and lies at its base, where the RWs are mounted on internal supports in the nearness of the outer shell.

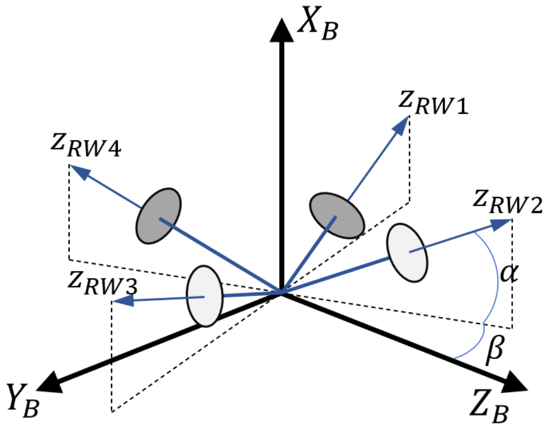

Figure 2.5. 4-Wheel Symmetric Pyramid RWA

Once the geometric configuration is known, it is possible with simple geometric considerations to express the mounting matrix from the local RWA frame to the spacecraft body frame, which will be used to transform the 4 torques provided or the angular moments of the RWs on the 3 body axes.

$$Z_w = \begin{bmatrix} \sin\alpha & \sin\alpha & \sin\alpha & \sin\alpha \\ -\cos\alpha\cos\beta & -\cos\alpha\sin\beta & \cos\alpha\cos\beta & \cos\alpha\sin\beta \\ -\cos\alpha\sin\beta & \cos\alpha\cos\beta & \cos\alpha\sin\beta & -\cos\alpha\cos\beta \end{bmatrix} \tag{2.35}$$

Thw RWA of the AOM has a configuration where $\alpha = 30°$ and $\beta = 45°$, and thus the mounting matrix becomes:

$$Z_w = \frac{1}{4}\begin{bmatrix} 2 & 2 & 2 & 2 \\ -\sqrt{6} & -\sqrt{6} & \sqrt{6} & \sqrt{6} \\ -\sqrt{6} & \sqrt{6} & \sqrt{6} & -\sqrt{6} \end{bmatrix} \tag{2.36}$$

2.7.2 Magnetorquers

Magnetotorquer is a widely used actuator, mainly employed for attitude control, detumbling, stabilisation and RW desaturation. By generating a magnetic dipole which interacts with a magnetic field, usually the Earth one, the magnetorquer is able to generate a torque. The magnetic dipole is created by small electromagnets generated by coils, and the intensity and direction of the torque depend on both the relative orientation of the magnetic field with respect to the magnetorquer and the current flowing in the coil.

Based on the number of magnetorquers present on the spacecraft, the total torque generated is obtained through the equation 2.37, where $\boldsymbol{M}$ comes from the addition of the magnetic moment contributions of the rods, and $\boldsymbol{B}$ is the external magnetic field.

$$\boldsymbol{T}_{MTQ} = \boldsymbol{M} \times \boldsymbol{B} \tag{2.37}$$

Space Rider is equipped with 3 magnetorquers directed along the body axes and they aren't used to control the spacecraft, given their limited authority, but are used as moment desaturators. In fact, the current spacecraft moment is compared with the expected one, and the MTQs deliver torque to compensate for the existing error. Moreover, the selected MTQs can only be deactivated or positively/negatively activated and for this reason, it's not possible a torque modulation.

Chapter 3

Guidance, Navigation and Control System

Space Rider missions will all be carried out in LEO. To guarantee a proper ground tracking and payload orientation, as well as an optimal orientation of the solar array, the attitude must undergo strict requirements, which are usually expressed in terms of accuracy, stability and agility. The Guidance, Navigation and Control is the subsystem in charge of fulfilling them.

This chapter gives a general introduction to the GNC subsystem, followed by a more detailed discussion of AOM's GNC. It concludes with an explanation of problems from which it may suffer.

3.1 Attitude Guidance and Control

Guidance is the part of the subsystem in charge of producing the desired profile of the manoeuvers, giving information regarding changes in position, velocity, attitude, and rates. The input of this subsection are data coming from navigation, and the output is the desired state which is delivered to the control. Guidance can be calculated on the ground and pre-loaded on a spacecraft or derived online. Moreover, online guidance can be performed both in open-loop and close-loop.

In the context of the thesis, the SRS attitude guidance will therefore be briefly described, as it is useful for understanding how attitude profiles are produced in simulations performed in Chapter 5.

AOM guidance at each instant calculates the LVLH orientation to determine Zenith and Nadir directions. Moreover, the Sun direction is estimated for the subsequent solar array Sun following. Hereafter are presented the main modes[1] that the system will be used in orbit.

- **Bay to Nadir/Zenith**
  It is an attitude keeping in which the MPCG is directed to Nadir/Zenith (figure 3.1), and the additional degree of freedom is used to expose the solar array toward the Sun in combination with the SADM. The control is performed by RWs, and the total pointing accuracy required is 0.05° (3σ).

- **Nose to out of plane**
  It is an attitude keeping in which the nose of the RM is in the direction of the orbital angular momentum (out of plane direction). The solar array is Sun following and RWs perform the control.

- **Tail to Sun**
  It is an attitude keeping in which the tail of SRS is directed toward the Sun. The solar array is Sun following, and RWs perform the control.

- **Slew**
  It is a manoeuvre which consists of a change of attitude from an initial state to a final one. Slew manoeuvers can be performed either in ECI or in LVLH reference frames. The guidance shall provide a manoeuvre compatible with RWs' capabilities.

Sun following is performed by using the Solar Array Drive Mechanism, which controls the SDAM angles. Thanks to the AOM attitude and to the SDAM, it is theoretically possible to always align the solar arrays perpendicular to the sunlight during manoeuvres. The perfect SUn following can be demanding for the actuators (especially for

---

[1] A basic manouvre/ attitude keeping function of the GNC

the low angles between the orbital plane and the Sun). In this case, it can be used an economic Sun following, which demands less control action from actuators.

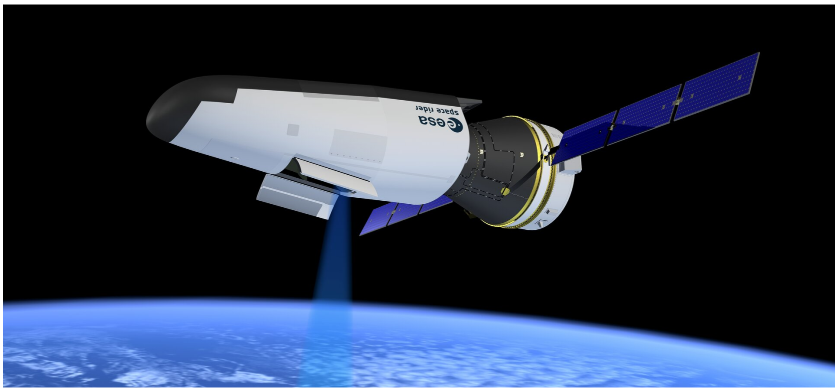

Figure 3.1. SRS Bay to Nadir orientation (credit: ESA [1])

Control is the part of the GNC in charge of commanding the actions performed by actuators based on the current and desired state. SRS's actuators, described and modelled in section 2.7, work together to ensure the fulfilment of requirements. RWs shall guarantee fine control, while MTQs are employed for unloading the wheels or eventually to control the attitude for the extreme micro-g environment. In fact, saturation implies an interruption of the desired manoeuvre/positioning and can be caused by either excessive torque demand or by the constant disturbance torque, such as gravity gradient or aerodynamic torque. The MTQs execute a continuous desaturation, through a bang-bang logic, which does not control the intensity of the commanded torque, but only the sign, thus only providing a torque that causes the angular momentum of the RW to decrease. If necessary, RACS can also be used to desaturate wheels.

The 3-axes commanded torque is computed using a PID controller (Proportional, Integrative, Derivative). Allocation to the 4 wheels is not carried out by simply using the assembly matrix Z_w, explicated in equation 2.36, but is subjected to an optimisation that refers to the approach proposed by Yoon [27]. Conventionally, torque optimisation exploits the minimum L_2 norm solution, which simply minimises the square sum of the torques, i.e. the total power required. The L_∞ norm, conversely, minimises the maximum absolute value of the individual torque and thus may be of greater interest for greater agility of the system. The disadvantage lies in the difficulty to express the L_∞ norm solution, which requires specific algorithms and can't be expressed in a closed form.

The solution proposed by Yoon exploits symmetries of the pyramid configuration with 4 identical RWs. The necessity to optimally redistribute the 3-axes torque to the 4 RWs arises from their limited torque and momentum capacities. For this reason, the goal is to postpone the wheel saturation as much as possible. This minimum L_∞ method enables the RWA to fully exploits its capacities during manoeuvres.

Let's define the L_∞ norm of a vector $\boldsymbol{v} = [v_1, ..., v_n]$ as

$$||\boldsymbol{v}||_\infty = max(|v_1|, ..., |v_n|) \tag{3.1}$$

Moreover, the 3-axes commanded total torque ($\boldsymbol{T}_t \in \mathbb{R}^3$) is usually distributed to the 4 wheels ($\boldsymbol{T}_w \in \mathbb{R}^4$) using the mounting matrix Z_w. This is also the solution that minimises the L_2 norm

$$\boldsymbol{T}_{w,L_2} = Z_w \boldsymbol{T}_t \tag{3.2}$$

For an under-determined linear equation like the one above, the solution can be rewritten as

$$\boldsymbol{T}_{w,L_\infty} = \boldsymbol{T}_{w,L_2} + \boldsymbol{T}_{null} \tag{3.3}$$

where $\boldsymbol{T}_{null}$ is the null vector wrt Z_w matrix, which satisfies the relation $Z_w \boldsymbol{T}_{null} = \boldsymbol{0}$. The vector can be expressed as follows

$$\boldsymbol{T}_{null} = \alpha * [T_{n,1}, ..., T_{n,4}]^T \tag{3.4}$$

where α is a real scalar and the vector and $[T_{n,1}, ..., T_{n,4}]^T$ is the null basis vector.

For a symmetric pyramid wheels configuration, the null basis is unitary and equal to $[1, 1, 1, 1]^T$, while the α than minimises the L_∞ norm is [27]:

$$\alpha = -\frac{min(\boldsymbol{T}_{w,L_2}) + max(\boldsymbol{T}_{w,L_2})}{2} \tag{3.5}$$

Because of the configuration adopted, the solution differs little from L_2 norm optimal one.

This solution can be furthermore optimised with some wheel angular momentum considerations. It is possible to minimise the L_∞ norm wrt the wheel speed vector from a given nominal speed. As presented before, let's call $\boldsymbol{H}_{w,L_2}$ the minimum L_2 norm commanded wheels' angular momentum. The scaling factor α has the same form as the one in equation 3.5 but with $\boldsymbol{H}_{w,L_2}$, and the null basis vector is again $[1,1,1,1,]^T$. The minimum L_∞ angular is therefore

$$\boldsymbol{H}_{w,L_\infty} = \boldsymbol{H}_{w,L_2} + \boldsymbol{H}_{null} \tag{3.6}$$

By comparing this result with the commanded angular momentum, it is possible to define the error in angular momentum $\Delta\boldsymbol{H}$. A PI-feedback law is then implemented to correct the torque with the integral and the proportional angular momentum error. The final commanded torque is:

$$\boldsymbol{T}_w = \boldsymbol{T}_{w,L_\infty} + K_P\Delta\boldsymbol{H} + K_I\int_{t_0}^{t}\Delta\boldsymbol{H}dt \tag{3.7}$$

3.2 Attitude Navigation

Navigation refers to the process of determination and/or estimation of the attitude and angular velocity of a spacecraft, by gathering and processing data from attitude sensors.

Attitude determination requires using three independent quantities to be fully resolute. In order to increase the reliability and robustness of the navigation phase, the use of estimators has become globally widespread. Attitude estimation differs from the determination both for the estimation, which is made of the attitude from the available measurements, and for the subsequent filtering of the noise. Methods available differ both in the system model used and in the propagation and filtering approach. Due to random errors and known ones of the sensors presented in Chapter 2, an accurate attitude is only achievable with the estimation approach.

However, attitude estimators are more prone to diverge because of uncertainties in models, spacecraft properties or in the external environment. It is then of utmost importance that increased performances are backed up by robust methods. An operable estimator shall guarantee that state estimation converges to the real state with a bounded error, in a finite and limited time.

For the purpose of this thesis, the Kalman filter and some of its derivations will now be presented.

3.2.1 Kalman Filter

The Kalman filter is an optimal estimator for the *linear quadratic problem* wrt any quadratic function. Specifically, the *linear quadratic problem* is the problem regarding the estimation of the states of a noisy linear system, by using noisy measurements. The Kalman filter was a cornerstone discovery of the *XX* century which has enabled numerous technological leaps forward in space, aviation and naval fields. The big breakthrough was the possibility of obtaining state estimates even in the lack of direct measurements, by means of indirect or noisy ones. Given a linear system with linear measurements, the KF is guaranteed to be the optimal filter: it minimises the estimation error in the least square sense. As stated before, the effectiveness of the estimation relies on the accuracy of the dynamic model and on the assumption that measurement and process noises are Gaussian white ones.

Let's consider the following dynamical system

$$\begin{cases} \dot{\boldsymbol{x}}(t) = f(\boldsymbol{x}(t), \boldsymbol{u}(t), t) + \boldsymbol{w}(t) \\ \boldsymbol{y}(t) = h(\boldsymbol{x}(t)) + \boldsymbol{v}(t) \end{cases} \tag{3.8}$$

where $\boldsymbol{x}(t)$ is the state vector, $\boldsymbol{u}(t)$ is the input vector, $\boldsymbol{w}(t)$ includes process noise and uncertainties, $\boldsymbol{y}(t)$ is the measurement vector and $\boldsymbol{v}(t)$ is the Gaussian white measurement noise. The non-linear dynamic model is $f(\boldsymbol{x}(t), \boldsymbol{u}(t), t)$, while the non-linear measurement model is $h(\boldsymbol{x}(t))$. The dimension of the state, input and measurement vector are respectively n, m and l.This system can be taken as a reference for describing the attitude dynamics of a spacecraft and in this case, the state vector includes both attitude (quaternions, Euler's angles, etc.) and angular velocities.

KF is applicable to linear systems. Let us assume that the system in equation 3.8 is linear. It can therefore be expressed by matrices in the following way

$$\begin{cases} \dot{\boldsymbol{x}}(t) = A(t)\boldsymbol{x}(t) + B(t)\boldsymbol{u}(t) + G(t)\boldsymbol{w}(t) \\ \boldsymbol{y}(t) = C\boldsymbol{x}(t) + \boldsymbol{v}(t) \end{cases} \tag{3.9}$$

where $A(t)$ is the state matrix, $B(t)$ is the input matrix, $G(t)$ is the process noise matrix and $C(t)$ is the observation matrix.

In the context of a mission, data from the sensors are provided in a discreet manner. Therefore, from now on the focus is on the discrete case. Let's call R the measurement noise covariance matrix and Q the process noise covariance matrix. Due to the hypothesis of Gaussian white noises, it results that

$$E[\boldsymbol{v}_k \boldsymbol{v}_k^T] = R_k \ , \ E[\boldsymbol{w}_k \boldsymbol{w}_k^T] = Q_k \tag{3.10}$$

R and Q express respectively how we can trust sensor measurements and how accurate is the model used. They are generally estimated at the beginning and then tuned experimentally. Moreover, let's define the error covariance matrix as

$$P_k = E[\widetilde{\boldsymbol{x}}_k \widetilde{\boldsymbol{x}}_k^T] \tag{3.11}$$

where $\widetilde{\boldsymbol{x}} = \boldsymbol{x}_k - \hat{\boldsymbol{x}}_k$ is the state error, $\boldsymbol{x}_k$ is the true state and $\hat{\boldsymbol{x}}_k$ is the state estimation. Kalman Filter estimations aim to minimise the trace of the error covariance matrix P at each step, in terms of mean square error.

KF is based on the following functioning: given $\hat{\boldsymbol{x}}_k^-$, *a priori* state estimation at time t_k, it search $\hat{\boldsymbol{x}}_k^+$, *a posteriori* state estimation based on the measurement $\boldsymbol{y}_k$, in the linear formulation

$$\hat{\boldsymbol{x}}_k^+ = K_k^x \hat{\boldsymbol{x}}_k^- + K_k^y \boldsymbol{y}_k \tag{3.12}$$

Matrices K_k^x and K_k^y are yet unknown. They must be chosen to ensure the optimum solution sought by the KF.

The *a priori* state estimation $\hat{\boldsymbol{x}}_k^-$ (prediction) is calculated through a state propagation of the estimation obtained in the previous step, using the system dynamic model

$$\hat{\boldsymbol{x}}_k^- = A_{k-1} \hat{\boldsymbol{x}}_{k-1}^+ \tag{3.13}$$

while, the *a priori* error covariance matrix is:

$$P_k^- = A_{k-1} P_{k-1}^+ A_{k-1}^T + Q_{k-1} \tag{3.14}$$

The *a posteriori* state estimation $\hat{\boldsymbol{x}}_k^+$ (update) requires finding the optimal solution of equation 3.15. The complete derivation of the problem can be found in [16, 28, 29]. The result is reported hereafter:

$$K_k^x = I - K_k^y C_k \tag{3.15}$$

By renaming for simplicity K^y as K, the *a posteriori* estimation becomes

$$\hat{\boldsymbol{x}}_k^+ = \hat{\boldsymbol{x}}_k^- + K_k(\boldsymbol{y}_k - C_k\hat{\boldsymbol{x}}_k^-) \tag{3.16}$$

and the *a posteriori* error covariance matrix

$$P_k^+ = (I - K_kC_k)P_k^-(I - K_kC_k)^T + K_kR_kK_k^T \tag{3.17}$$

The diagonal of the covariance matrix consists of the mean square errors, and to minimise them, it is necessary to minimise the trace. This leads the problem of finding the K-matrix back to a minimisation problem. By differentiating the trace wrt K_k and equating it to zero, the minimum is found as

$$K_k = P_k^- C_k^T (C_k P_k^- C_k^T + R_k)^{-1} \tag{3.18}$$

which is called the Kalman gain matrix.
The sequential steps of the procedure are as follows:

1. Compute P_k^- using P_{k-1}^+, A_{k-1} and Q_{k-1}
2. Compute the Kalman gain K_k using P_k^-, C_k and R_k
3. Compute P_k^+ using K_k and P_k^-
4. Compute $\hat{\boldsymbol{x}}_k^+$ using K_k, the measurement $\boldsymbol{y}_k$ and $\hat{\boldsymbol{x}}_k^-$ or the initial condition $\boldsymbol{x}_0$

KF has two main limitations: it assumes that both system and observation model equations are linear, which is not realistic in many real-life situations, and it assumes that noises are Gaussian distributed: it will act then as an optimal estimator under this statistical distribution otherwise it will be only a linear minimum estimator.

3.2.2 Extended Kalman Filter

Due to the non-linearity present in many dynamic systems, the KF cannot be directly applied. It has been designed to estimate states in a linear model. This limitation can easily be overcome by linearising the system and the observation function in the current position. The idea is pretty common and natural, but the filtering procedure becomes far more efficient. This approach is called Extended Kalman Filter. In the space sector, due to the many non-linearities encountered, the EKF has met with great success and is still one of the most reliable and widely used algorithms despite being introduced more than 50 years ago.

Let's consider the non-linear system reported in equation 3.8. System and observation equations are non-linear, and noises have a Gaussian distribution. Non-linear functions are linearized using a first-order Taylor series expansion at $\hat{\boldsymbol{x}}_k$ for $f_k(\boldsymbol{x}_k)$ and at $\hat{\boldsymbol{x}}_k^-$ for $h(\boldsymbol{x}_k)$.

$$\begin{cases} f_k(\boldsymbol{x}_k) \simeq f_k(\hat{\boldsymbol{x}}_k) + A_k(\boldsymbol{x}_k - \hat{\boldsymbol{x}}_k) \\ h_k(\boldsymbol{x}_k) \simeq h_k(\hat{\boldsymbol{x}}_k^-) + C_k(\boldsymbol{x}_k - \hat{\boldsymbol{x}}_k^-) \end{cases} \tag{3.19}$$

Where

$$A_k = \left[\frac{\partial f_k}{\partial \boldsymbol{x}_k}(\hat{\boldsymbol{x}}_k)\right] \tag{3.20}$$

$$C_k = \left[\frac{\partial h_k}{\partial \boldsymbol{x}_k}(\hat{\boldsymbol{x}}_k^-)\right] \tag{3.21}$$

The linearized equations have the same form as the KF ones, with the difference that the linearization is performed at each estimation step, with the consequence of having to calculate the Jacobian at each step time. Besides these differences in the matrices to be used, equations are exactly the same as those presented in section 3.2.1 for the classical Kalman Filter.

By linearizing at each step, errors can be sensibly reduced and one can move significantly from the initial conditions without the estimate diverging. The main drawback of this procedure is the higher computational load required for the linearization at each step. As for the KF, the convergence of results is strictly related to the fidelity of the implemented models and to the choice of the initial condition. Moreover, EKF is not an optimal estimator for non-linear systems, while the KF is an optimal estimator for linear ones.

3.2.3 Space Rider MEKF

Space Rider AOM attitude navigation uses measurements provided by STRs (attitude) and IMU (angular velocity), as described before. Specifically for attitude estimation, the IMU information (measured angular rate) is used continuously (at high frequency) to propagate quaternions over time. The other measurements of attitude are used to update the estimated attitude. These other measurements occur at a lower frequency and can be absent for a given duration (blinding, etc.). The filter used for attitude is the so-called Multiplicative Extended Kalman Filter.

The non-linear quaternion expression in MEKF is composed of a unit reference quaternion $\boldsymbol{q}_{ref}(t)$ and a unit quaternion $\delta\boldsymbol{q}(\boldsymbol{a}(t))$ representing the rotation between $\boldsymbol{q}_{ref}(t)$ and the true attitude $\boldsymbol{q}(t)$. The $\delta\boldsymbol{q}(\boldsymbol{a}(t))$ is parametrised through a three-component Gibbs vector $\boldsymbol{a}(t)$ for error management. The basic idea of the MEKF is to calculate a "local" unconstrained estimate of the 3x1 state vector $\boldsymbol{a}(t)$ while using the correctly normalised four-component $\boldsymbol{q}_{ref}(t)$ to obtain a non-singular "global" attitude representation [11].

The decision to use this algorithm came down to its remarkable stability. Moreover, it is worth highlighting that the covariance matrix of the quaternion representation is singular and it is not straightforward to be interpreted. By using a three-dimensional vector representation, the covariance matrix becomes non-singular and it has a far more obvious physical interpretation.

The equations used by this algorithm are similar to those of the EKF, except that MEKF updates the error state and not the global state as the EKF does. Complete coverage of the problem, which goes beyond the purpose of this thesis, can be found in [11, 30, 31]

3.3 Problems affecting Space Rider AOM GNC

After the generic description of the GNC subsystem and deriving it for the specific case of the Space Rider AOM, the related issues considered in the thesis work are now introduced specifically.

3.3.1 Star trackers

A Star Tracker is one of the most accurate attitude sensors in the space sector. Performances are strongly related to the size of the sensor as well as to mission purpose, but it is clear that to achieve very precise measurements, all uncertainties must be minimised.

STR measurement performances can be affected by two main problems: one related to the correct calibration of the instrumentation required for photo acquisition and the other one concerning the misalignment of the instrument itself with respect to the nominal orientation.

The first one includes geometric deflections of lenses and other camera parameters which can affect images captured. For this type of problem, there are many works in the literature that allow successful onboard calibrations for different problems that can be encountered.

On the other hand, misalignments of STRs are easier to handle, as they do not require specific algorithms. The main difficulty lies in ensuring that methods used for identifying and then compensating for misalignments are robust to system uncertainties, external factors and unknown parameters.

In the specific case of Space Rider, the study of misalignments is of paramount importance for the very conformation of the spacecraft. It's useful to remember that the AOM is the module in charge of handling all the orbital GNC activities, but the MPCG and thus payloads are inside the re-entry module. It is thus clear that for the purpose of the mission, the orientation of the cargo bay must be precisely determined, but two out of three STRs are mounted on the side of the AOM, and therefore at a distance of a few metres. This distance causes any structure release in orbit, thermal deformations or launch solicitations, to alter the nominal orientation of equipment, and consequently also the relative orientation between the STR and the MPCB. It is therefore necessary to carry out a characterisation along the orbit of the misalignments at the beginning of the mission, to ensure the reliability of the data obtained from all three STRs, and not just of the one inserted in the MPCB. The final aim of the work is to be able to guarantee data continuity with the same accuracy level even during the blinding conditions of the STR inserted in the MPCG which, depending on the mission timeline type, can also be long-lasting.

3.3.2 Reaction Wheels

In the first decades of space missions, many missions failed due to actuator problems. These accidents made it necessary to study and develop Fault Tolerant Control. The demanding mission requirements of SRS mandate the implementation of a FTC. Specifically, problems related to RW, the main actuator for attitude control, will be discussed and then described.

It is worth remembering that a RW is composed of a flywheel driven by an electric motor, with a bearing and the required electronics. RWs shall rotate in either direction within the operational limits for their entire life. First of all, bearings must be long-lasting and their lubrication has to be optimal even in the space environment. In addition, electronics must also ensure a nominal operating life. These are the components most prone to failure. The combination of their partial or total faults can generate the following RW's malfunctioning [32]:

1. *Failure to respond to control signals.* This failure leads the wheel to hold its speed without responding to control signals. The causes of the failure are faulty drive electronics, drive motor or power supply or a break in the wires and grounding of the electrical inputs/outputs.

2. *Decreased reaction torque.* Given a torque control signal, the torque reaction torque generated is less than expected due to a lower rate of change of speed. The main causes are the increased friction in the bearing due to inadequate lubrication, change of lubricant properties or the decrease in the current drive.

3. *Increased bias torque.* This failure takes place when the control signal is zero, but the RW generates torque. But, because of changes in friction magnitude (ageing of bearing, temperature cycles, etc.), the wheel may not hold its speed. This gradual variation in speed produces a low reaction torque, known as bias torque.

4. *Continuous generation of reaction torque.* Failures in electronics might cause a continuous increase or decrease in the wheel's speed, generating thereby a reaction torque.

While some failures require to switched off the RW due to the total unpredictability of the behaviour (faults 1 and 4), others can be counteracted. Specifically, the work of this thesis focuses on the identification and compensation of failures related to the decrease in the reaction torque: they can occur for different causes and with different severities, and they are the most frequent type of failure.

Chapter 4

Identification and compensation methods

This chapter describes all the algorithms and methodologies applied to solve the GNC problems introduced in chapter 3. Firstly, however, a generical description of the Sliding Mode is provided, with particular attention to Sliding Mode Observers, having made extensive use of them in the prosecution of the thesis.

4.1 Sliding Mode Observer for off-nominal behaviours and misalignments

Sliding Mode is a technique which originated from the theory of Variable Structure Systems. In the formulation of control problems, it is usual to have discrepancies between the model used and the real plant, and this leads to considering robust control. Sliding Mode controls began to be applied in complex systems subject to uncertainties. The idea behind this is to control the dynamics of a system by injecting a discontinuous input which forces the system to reach the sliding surface in finite time and subsequently stay on it. The advantages provided are the robustness wrt system and external uncertainties, a finite-time convergence and reduced-order compensated dynamics.

Sliding Mode Observers still exploit sliding surfaces but for a different purpose: estimating the states of a system using measured input and/or output. They potentially ensure the same advantages as the ones of the controllers, such as robustness to uncertainties and finite time precise estimations. The main drawback of the sliding mode is chattering, which arises as a direct consequence of the discontinuous injection term.

An observer consists of a mathematical replica of a system, in which are included input and a signal that represents the difference between observer output and measured output, namely the injection term. First observers originated from the studies of Luenberger, and they made use of a linear injection term, which was directly injected in feedback into the system. A Luenberger observer works properly with well-known systems. In presence of uncertainties and unknown signals, these observers are unable to take the estimation error to zero, and thus output states are not able to converge to system states. The non-linear injection term used by SMO can conversely force the estimation error to become zero in finite time. Apart from the tuning of observer parameters to guarantee finite time convergence, the only condition for the applicability of the SM is to have systems whose disturbances are bounded in magnitude.

To better understand how the SMO works, some examples of first-order and higher-order observers are now presented.

4.1.1 First Order Observer

Let's consider the following classical linear system

$$\begin{aligned} \dot{x}(t) &= Ax(t) + Bu(t) \\ y(t) &= Cx(t) \end{aligned} \tag{4.1}$$

where the matrices are the same of those in equation 3.9, $x(t)$ represents the state, $u(t)$ is the input while $y(t)$ is the output. In the end, the purpose of the observer is to estimate the state variable $x(t)$ by making use of the information contained in $u(t)$ and $y(t)$.

The simplest first-order SMO that can be applied to the system in equation 4.1, and it is described by the following equations

$$\begin{aligned}\dot{\hat{x}}(t) &= A\hat{x}(t) + Bu(t) + L\nu \\ \hat{y}(t) &= C\hat{x}(t)\end{aligned} \tag{4.2}$$

where L is a gain matrix to be determined, $\hat{x}(t)$ is the state estimation, $\hat{y}(t)$ is the output estimation and ν is the discontinuous injection term. The latter can be defined in the simplest way as follows

$$\nu = \rho \cdot sign(e_y) \tag{4.3}$$

where $e_y(t) = \hat{y}(t) - y(t)$ is the output estimation error, and ρ is a positive scalar. Similarly, it's possible to define $e_x(t) = \hat{x}(t) - x(t)$ as the state estimation error. In this case, the injection term ν is chosen with respect to the sliding surface $S = \{e_y : Ce_y = 0\}$, in order to force $e_y(t)$ towards S in a finite time and then make it stick on it. This is known as the *sliding condition* (figure 4.1) which is the condition sought by any kind of sliding mode, whether observer or controller.

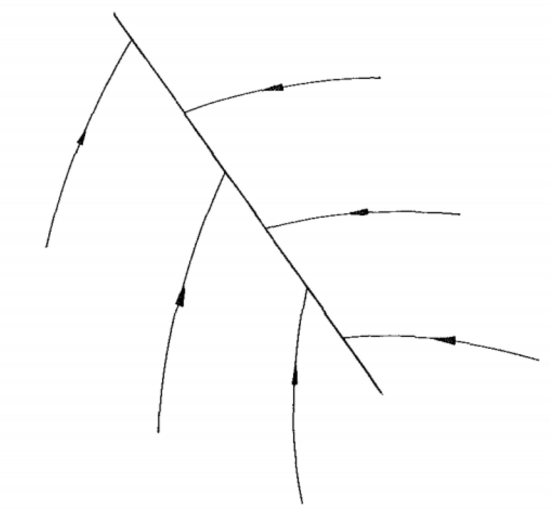

Figure 4.1. The sliding condition [33]

To ensure convergence of the SMO, it is necessary to choose properly ρ. Based on the initial conditions, it is necessary to define which scalar guarantees convergence. Normally, the optimal choice that ensures robustness is made following a study of the conditions under which the system will operate. As a general behaviour, the smaller the parameter becomes, the more convergence may not be guaranteed [2]. Conversely, the higher the ρ parameter becomes, the more likely the chatter phenomenon might arise.

As mentioned earlier, chattering is in fact one of the main problems affecting SM and SMO. It can be described as high-frequency oscillations of states or state estimations occurring around the sliding surface. Over the years, numerous methods have been proposed to overcome this problem. They mainly involve the substitution of the $sign(e)$ function with other functions that approximate the discontinuity of $sign$, when $e \to 0$, in a smoother way.

The most widespread examples of these functions, for instance, are the saturation function

$$sign(e) \approx \begin{cases} 1 & if\ e > \epsilon \\ e/\epsilon & if\ |e| \leq \epsilon \\ -1 & if\ e < -\epsilon \end{cases} \tag{4.4}$$

or the sigmoid function

$$sign(e) \approx \frac{e}{|e| + \epsilon} \tag{4.5}$$

where ϵ is a positive scalar to be properly chosen based on the formulation of the problem. Once again, as a general rule, it is known that the more the discontinuity is reduced, the more the SM tends to lose rapidity and robustness to parameter uncertainties. This behaviour is predictable: by smoothing out the discontinuity that differentiates the SMO from linear ones, its behaviour will tend to become increasingly closer to the latter.

Due to the fact that an improvement in chattering leads to the loss of other essential SM properties, this drawback has been overcome over the years with the introduction and the use of higher-order SMO. Thanks to a different formulation and a greater number of parameters, higher-order SMO are able to deal more efficiently with a wider variety of systems.

4.1.2 Higher-Order Observer

In addition to the above-mentioned advantages of the first-order SMO, higher-order ones can be moreover applied to systems with a relative degree greater than one achieving exact results. This becomes a crucial aspect in dealing with both the attitude and the position dynamics of an orbiting spacecraft, which is in fact a dynamics of relative degree two.

The observer proposed and used in this thesis is based on the super-twisting algorithm. Historically, the super-twisting algorithm is the first second-order sliding mode algorithm introduced. The main difference if compared with the first-order one it is the twisting motion around the origin of the second-order sliding variable (figure 4.2). In this case, the sliding surface can be defined as $S = \{e : \dot{e} + Ce = 0\}$, and the aim is to bring states and state derivatives on it and make them stay there. For this reason, the observer problem in two dimensions can be described as the action to force the state estimations to converge towards the sliding surface in a finite time, performing this time rotations around it. This rotary motion is comparable to chattering in one dimension: a high-frequency oscillation around the sliding surface.

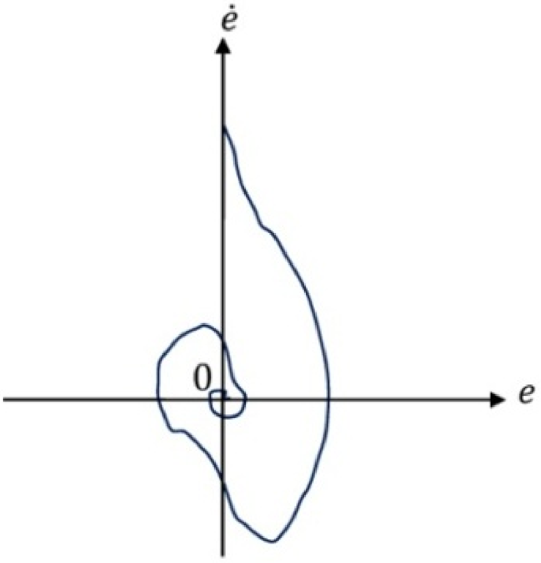

Figure 4.2. Super-twisting sliding condition [34]

Let's consider the following time-varying second-order non-linear system

$$\begin{cases} \dot{x}_1 = x_2 \\ \dot{x}_2 = f(t, x_1, x_2, u) + d(t) \end{cases} \tag{4.6}$$

where x_1 and x_2 are the states, specifically a state and its derivative, u the input, $f(t, x_1, x_2, u)$ the non-linear system function and $d(t)$ the unknown but bounded disturbance. Moreover, let's suppose we are able to measure the state x_1 by means of some sensors, and thus have the measurement y_1.

The super-twisting observer applied to the system in equation 4.6 has the following form

$$\begin{cases} \dot{\hat{x}}_1 = \hat{x}_2 + z_1 \\ \dot{\hat{x}}_2 = f(t, \hat{x}_1, \hat{x}_2, u) + z_2 \end{cases} \tag{4.7}$$

where $\hat{x}_1$ and $\hat{x}_2$ are the state estimations, and z_1 and z_2 are the discontinuous injection terms, which have the following formulation:

$$z_1 = \lambda |\widetilde{x}_1|^{1/2} sign(\widetilde{x}_1) \tag{4.8}$$

$$z_2 = \alpha \ sign(\widetilde{x}_1) \tag{4.9}$$

The new term $\widetilde{x}_1 = y_1 - \hat{x}_1$ is the estimation error, the difference between the measurement and the state estimation. The super-twisting observer allows for exact results dealing with spacecraft dynamics of relative degree two.

An immediate way to discuss the convergence of the method begins by first obtaining the error equations:

$$\begin{cases} \dot{\widetilde{x}}_1 = \widetilde{x}_2 + \lambda |\widetilde{x}_1|^{1/2} sign(\widetilde{x}_1) \\ \dot{\widetilde{x}}_2 = F(t, x_1, x_2, \hat{x}_1, \hat{x}_2, u) + \alpha \ sign(\widetilde{x}_1) \end{cases} \tag{4.10}$$

The term $\widetilde{x}_2 = x_2 - \hat{x}_2$ is the second state error of which the measurement is not available, and $F(t, x_1, x_2, \hat{x}_1, \hat{x}_2, u) = f(t, x_1, x_2, u) + d(t) - f(t, \hat{x}_1, \hat{x}_2, u)$. Let's suppose that the system states are bounded: this is for instance a plausible assumption for spacecraft dynamics, addressed in part of the thesis. It is consequently ensured the existence of a constant C which satisfies the following linear inequality:

$$|F(t, x_1, x_2, \hat{x}_1, \hat{x}_2, u)| < C \tag{4.11}$$

Once this constant is derived, it is consequently possible to calculate the following two parameters

$$\alpha > C \tag{4.12}$$

$$\lambda^2 \geq 4C\frac{\alpha + C}{\alpha - C} \tag{4.13}$$

It can be demonstrated that if the parameters of the super-twisting observer presented in equations 4.7 are chosen according to equations 4.12 and 4.13, and the condition introduced in equation 4.11 holds for the system, the finite-time convergence of the states is guaranteed. Specifically, this means bringing estimation errors to zero in finite time, i.e. $\widetilde{x}_1 = 0$, $\dot{\widetilde{x}}_1 = 0$. This is a sufficient condition to guarantee convergence for the proposed second-order super twisting SMO [8]. For the sake of completeness, the constant C is called Lipschitz's constant[1].

Although tuning appears straightforward, it must be borne in mind that it is not always possible to have a detailed representation of the system, contained in the system function F. In particular, parameter uncertainties and external disturbances could make the procedure difficult. But in parallel, if the mathematical model is known with sufficient precision, it is possible to carry out an estimation of system parameters and/or uncertainties. This procedure is of high interest for the identification of off-nominal RW behaviours, for which it was designed a dedicated system observer in sub-section 4.2.2.

In this overview, the state function of the system reported in 4.7 is deliberately unspecified, as are the state variables. They will be detailed in sections 4.2.1 and 4.2.2, where SMOs are applied to case studies, but precisely it is nothing more than the equations of dynamics with relative variables in one case, and an *ad hoc* system for observing RWs in the other.

---

[1] Given a function $f : [a, b] \to \mathbb{R}$, the Lipschitz's constant C is the smallest constant satisfying the linear inequality $|f(x) - f(x')| \leq C|x - x'|$, $\forall x,\ x' \in \mathbb{R}$, which is furthermore called the Lipschitz condition.

4.2 Compensation of off-nominal behaviours and misalignments

Hereafter are presented the methodologies applied for GNC off-nominal behaviours and misalignments, using Sliding Mode Observers combined with other algorithms,

4.2.1 Star tracker misalignments

The problem to be solved, presented in sub-section 3.3.1, consists of a more complex first identification part, while the compensation one is straightforward. The greatest concern is to obtain an attitude estimation accurate enough to actually be able to identify these misalignments.
The attitude estimation method used is based on a super-twisting SMO, which will be then compared to a classical EKF-based observer in chapter 5 to demonstrate the enhanced performances.

Misalignment Identification

The proposed observer derived from the one presented in equation 4.7, where non-linear system function $f(t, \hat{x}_1, \hat{x}_2, u)$ is nothing other than the equation of the spacecraft attitude dynamics already reported in equation 2.19. By adapting the equation to actuators available on SRS (i.e. RWs and MTQs), the observer equations become as follow

$$\begin{cases} \dot{\hat{\boldsymbol{\theta}}} = \hat{\boldsymbol{\omega}}_B + \lambda |\boldsymbol{y} - \hat{\boldsymbol{\theta}}|^{1/2} sat(\boldsymbol{y} - \hat{\boldsymbol{\theta}}) \\ \dot{\hat{\boldsymbol{\omega}}}_B = -J^{-1}(\hat{\boldsymbol{\omega}}_B \times (J\hat{\boldsymbol{\omega}}_B + \boldsymbol{H}_w) + \boldsymbol{T}_w - \boldsymbol{T}_{ext}) + \alpha \; sign(\boldsymbol{y} - \hat{\boldsymbol{\theta}}) \end{cases} \tag{4.14}$$

Specifically, the state variables used are clearly the estimated angular velocity in body frame $\hat{\boldsymbol{\omega}}_B$, and the spacecraft attitude expressed through the Euler's angles parametrization, $\hat{\boldsymbol{\theta}}$. Furthermore, $\boldsymbol{y}$ is the measurement vector coming from STRs, expressed also with Euler's angles. It is worth pointing out that the relationship between the derivative of the Euler's angles and the angular velocity is the one reported in equation 2.13. In the system 4.14 the matrix relating the two quantities is neglected, as the non-linear injection term, due to its discontinuity, provides compensation for both this discrepancy and any other model discrepancy or uncertainty. The reason for using it can be derived from what was written above: given the intrinsic constitution of the SMO, it is preferable to have an attitude parameterization that directly correlates with the angular velocity rather than a more complex one, such as quaternions for example, whose correlation with angular velocities is conversely more complex to express.

In addition, numerous tests and simulations were carried out to select the most suitable SMO version for this system and for these operating conditions. In the end, it turned out that the use of the saturation function instead of the sign one in the first equation of the system reported in 4.14 was the best choice, in order to obtain smoother and more accurate results.

The theoretical discussion about convergence and stability of the super-twisting approach is fully covered in [8]. The condition for a finite-time convergence presented before in equations 4.12 and 4.13 are the only conditions worthy of consideration for the purpose of this thesis.

Misalignment correction

Once an estimate of the spacecraft attitude with the two different STRs has been obtained (the reference one, and the one subject to misalignment), the compensation phase is articulated as follows:

1. It is necessary to use the attitude estimation of the reference STR ($\boldsymbol{q}_{STR_{ref}}$) and the one of the STR potentially subject to misalignment ($\boldsymbol{q}_{STR}$) and calculate the misalignment between the twos.

$$\boldsymbol{q}_{mis} = \boldsymbol{q}_{STR_{ref}}^{-1} \otimes \boldsymbol{q}_{STR} \tag{4.15}$$

2. Established that the discrepancy is caused by misalignment of the STR wrt its nominal mounting direction and not just from instrument errors, the faulty measurement is simply corrected with a rotation equal and opposite to the measured error calculated above.

$$\boldsymbol{q}_{STR_{corr}} = \boldsymbol{q}_{STR} \otimes \boldsymbol{q}_{mis}^{-1} \tag{4.16}$$

4.2.2 Reaction Wheel off-nominal behaviours

The second identification and compensation problem addressed, previously presented in sub-section 3.3.2, is more complex and consists of several steps, both in the identification part and in the compensation part. In order to provide an overview of the logic used, a representative block diagram of the logic of the algorithm used is shown in figure 4.3.

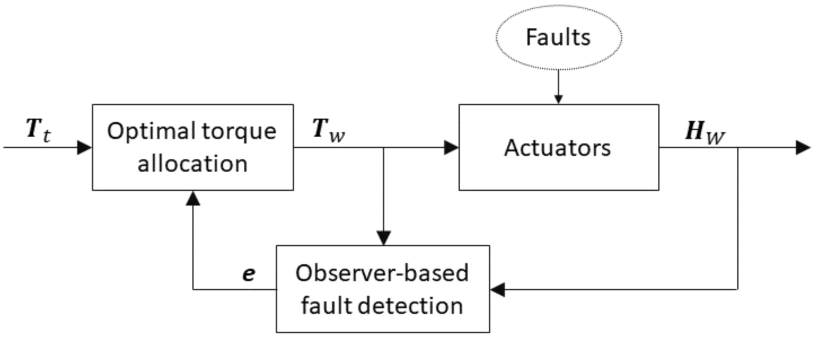

Figure 4.3. Structure of the RWs applied method

In particular, it represents a portion of the scheme of the GNC, i.e. the one involved in the study carried out. The parameters reported and used in the algorithms are the commanded total control input $\boldsymbol{T}_t \in \mathbb{R}^3$ in body-axes, the commanded torque to the 4 wheels $\boldsymbol{T}_w \in \mathbb{R}^4$ and the wheels' angular momentum $\boldsymbol{H}_w$, which is derived directly from tachometer measurements of the angular velocity of the wheels. Moreover, one of the most important parameters of the analysis is e, the parameter that denotes the efficiency of the RW, and it's defined as follows:

$$e_i = \frac{T_{act_i}}{T_{cmd_i}} \tag{4.17}$$

Consequently, it is possible to introduce a new matrix defined as $E_w = diag(\boldsymbol{e})$, which is diagonal and has the efficiencies of the RWs on the diagonal. Being e_i bounded between the lower value 0 and the upper value 1, E_w results to be a positive-definite matrix, and it will be also referred to as the weighting matrix in the torque allocation problem.

The logic of the implemented algorithm can be divided into two steps: firstly, it is necessary to identify actuators that have a off-nominal functioning. Subsequently, the 3-axes commanded torque is redistributed to the 4 actuators taking into account the faulty ones, and aiming to reduce their use. A detailed description of the complete procedure is given hereafter.

Failure Identification and Reconstruction

The problem of RW fault diagnosis can be divided into a first failure identification step based on the output parameters and system models, and a following reconstruction of the unknown parameters.

The identification phase makes use again of a SMO. Starting from the available measurements, i.e. those of the angular momentum of the wheels $\boldsymbol{H}_{w_{meas}}$, the aim is to estimate the torque produced by the RWs. The observer proposed is the one described in [33] for second-order dynamic systems ($\ddot{x}_1 = f$), when only a single measurement is available to the system (y_1):

$$\begin{cases} \dot{\hat{\boldsymbol{x}}}_1 = \hat{\boldsymbol{x}}_2 + k_1 sign(\boldsymbol{H}_{w_{meas}} - \hat{\boldsymbol{x}}_1) \\ \dot{\hat{\boldsymbol{x}}}_2 = k_2 sign(\boldsymbol{H}_{w_{meas}} - \hat{\boldsymbol{x}}_1) \end{cases} \tag{4.18}$$

For ease of writing, the parameters used are $\hat{\boldsymbol{x}}_1 = \hat{\boldsymbol{H}}_w$, the estimation of the wheels angular momentum, and $\hat{\boldsymbol{x}}_2 = \dot{\hat{\boldsymbol{H}}}_w$, the estimation of the derivative of wheels angular momentum. With this variable choice, it is possible to obtain a set of state estimates which are less prone to fluctuation following a more linear evolution. It is worth remembering that angular momentum is closely linked to the rotational speed of the wheel ($\boldsymbol{H}_{RW} = I_{RW}\boldsymbol{\omega}_{RW}$), and made exception of breakage, it is very unlikely having large instantaneous changes in the angular momentum. Knowing that the torque is in fact the derivative of the angular momentum, and on which instantaneous variations are usual, it is easier to identify any off-nominal behaviour from the study of angular momentum, even though the output required is the actuated torque $\boldsymbol{T}_{act}$. To summarise, it is studied the angular momentum and only ultimately the actuated torque is obtained through a derivation, rather than directly studying the torque prone to intrinsic greater errors.

To define the wheel efficiency parameter $\boldsymbol{e}$ in a meaningful way, it is necessary to make some considerations about how the commanded torque changes due to the real effects of the RW equipment. It is of utmost importance to determine in orbit whether the discrepancy results from known and expected effects of RWs or whether they are indices of malfunctioning. In order to achieve satisfying results without excessively increasing the computational load, it is used a simplified model of the RW to include the real main effects. These are friction (particularly Coulomb and viscous effects) and wheel saturation. Other secondary and less influential effects are neglected (i.e. Striebeck effect, wheel imbalances, windage and magnetic losses, etc.). By using this simplified model, the commanded torque is thus pre-filtered, obtaining an estimated commanded torque $\boldsymbol{T}_{est}$, which is the one that will actually be used to calculate the efficiency parameter:

$$e_i = \frac{T_{act_i}}{T_{est_i}} \tag{4.19}$$

Before considering the reconstruction of the failure concluded, it is necessary to go into some detail about the implemented algorithm and the inherent limitations of the problem formulation itself.

- Due to intrinsic oscillations induced by the SMO, the efficiency parameter is filtered with a moving average over $1s$ of simulation, in order to achieve smoother estimations.
- When the actuated torque is close to zero ($|T_{act}| < 10\% T_{max}$), model uncertainties might lead to possible sign discrepancies between estimated and actuated torque, and consequently to a loss of meaning of the efficiency parameter, and thus is not calculated

Optimal Torque Redistribution

The commanded 3-axes torque coming from the controller has to be redistributed to actuators taking into account estimated faults, specifically through $\boldsymbol{e}$, by means of a reconfiguration closed-loop routine, which is external to the controller (i.e. it does not need to be reconfigured if efficiency decreases are identified). The algorithm is described below.

$\boldsymbol{T}_t$ can be expressed as a linear combination of $\boldsymbol{T}_w$, the torque of single RWs, as mentioned in the subsection 2.7.1, and reported for completeness hereafter:

$$\boldsymbol{T}_t = Z_w \boldsymbol{T}_w \tag{4.20}$$

The commanded torque of every wheel can be derived by manipulating equation 4.20, obtaining

$$\boldsymbol{T}_w = Z_w^{\dagger} \boldsymbol{T}_t \tag{4.21}$$

where $Z_w^{\dagger}$ is the pseudo-inverse matrix of the mounting matrix Z_w, which satisfies the equality $Z_w Z_w^{\dagger} = I_3$. The choice of $Z_w^{\dagger}$ is therefore not unique, and it can be selected in several ways. The choice was made in order to minimise at each step the following minimisation problem:

$$\min_{\boldsymbol{T}_w} (\boldsymbol{T}_w^T E_w^{-1} \boldsymbol{T}_w) \;\; \text{subject to} \;\; \boldsymbol{T}_t = Z_w \boldsymbol{T}_w \tag{4.22}$$

The problem presented above aims to minimise the sum of squares cost related to the RWs commanded torque $\boldsymbol{T}_w$, weighted by E_w. The optimal solution to the problem is given by

$$Z_w^{\dagger} = E_w Z_w^T (Z_w E_w Z_w^T)^{-1} \tag{4.23}$$

When a loss of efficiency occurs, E_w is no more equal to the identity matrix, and so the control effort is reallocated trying to minimise the use of the faulty actuator, which is also more prone to unexpected and potentially harmful behaviour since it does not function nominally. At each step, the pseudo-inverse matrix $Z_w^{\dagger}$ is calculated, and T_t is redistributed without the necessity to redesign the controller.

It is worth noting that in a fault-free condition, when the weighting matrix is equal to the identity matrix I, the $Z_w^{\dagger}$ matrix results to be the classical Moore-Penrose pseudo-inverse.

As a final step, each RW commanded torque T_{w_i} is rescaled by a factor $1/e_i$, to minimise the mismatch between commanded and actuated torque. This action, being carried out after the controller, makes it possible to obtain an actuated torque similar to that commanded one, thus minimising the discrepancy and consequently not having unexpected system behaviour.

Chapter 5

Simulation results

This chapter contains analyses performed to test the effectiveness of the proposed algorithms. The two GNC problematics introduced and explained in the previous chapters are addressed separately, making use of the same simulator. The chapter ends with the thesis conclusions and a discussion about possible future works.

Analyses were carried out using MATLAB & Simulink environment, in a simulator that takes into account attitude and orbital dynamics. Sensor and actuator parameters are those reported in chapter 2, while inertial properties of SRS used during analysis are reported in the following inertia matrix:

$$J = \begin{bmatrix} 3163 & 69 & -155 \\ 69 & 2322 & 175 \\ -155 & 175 & 2146 \end{bmatrix} kg \cdot m^2 \tag{5.1}$$

Although the calculations were performed using quaternions, the results are reported using 321-Euler's angles parameterization, for their ease of visualisation.

5.1 Star Tracker misalignments

The proposed algorithms in section 4.2.1 are applied to a real situation that SRS will face in the operative life. But before proceeding with the presentation of the results, it is necessary to explain the setting of the simulation performed.

For the reasons listed in the sub-section 3.3.1, STR misalignment can be represented as consisting of two main contributions:

1. A constant misalignment due to mounting errors, zero-g release, vibrations, etc.
2. A variable misalignment along the orbit, mainly caused by thermo-elastic deformations given by transitions between eclipse and non-eclipse conditions.

Moreover, results of thermo-structural studies carried out previously report that the maximum single-axis rotation error between the MPCB and STRs support is 0.04°. In the proposed simulation, a single STR is analysed. It is assumed that the STR have a constant misalignment per axis in the range of $-0.04° \leq \theta \leq 0.04°$ and a variable misalignment eclipse time, whose value at steady state is again between $-0.04° \leq \theta \leq 0.04°$. The values on the three axes are chosen randomly, due to the unpredictability of situations that may occur in orbit.

Assuming that the maiden mission will be launched at the end of 2024, the following simulation reproduces a B2N attitude keeping lasting one orbit, on January the 1st 2025. The orbit is circular, has a height of $400km$ and is inclined of 7°. This information is necessary to understand when the spacecraft is in eclipse or not, and therefore when thermo-elastic deformations change. Figure 5.1 shows the misalignment along the orbit imposed on the STR support, expressed in the STR local reference frame.

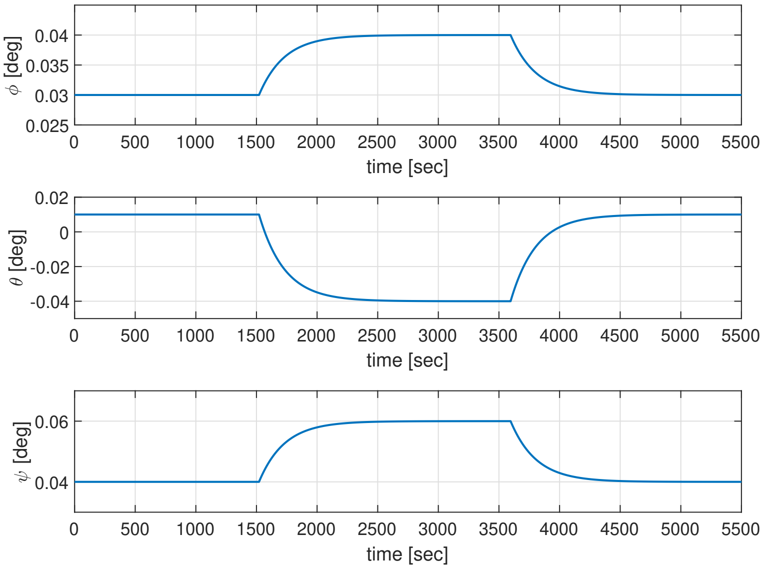

Figure 5.1. STR misalignment along the orbit

Hereafter are then reported the true states of the B2N attitude keeping.

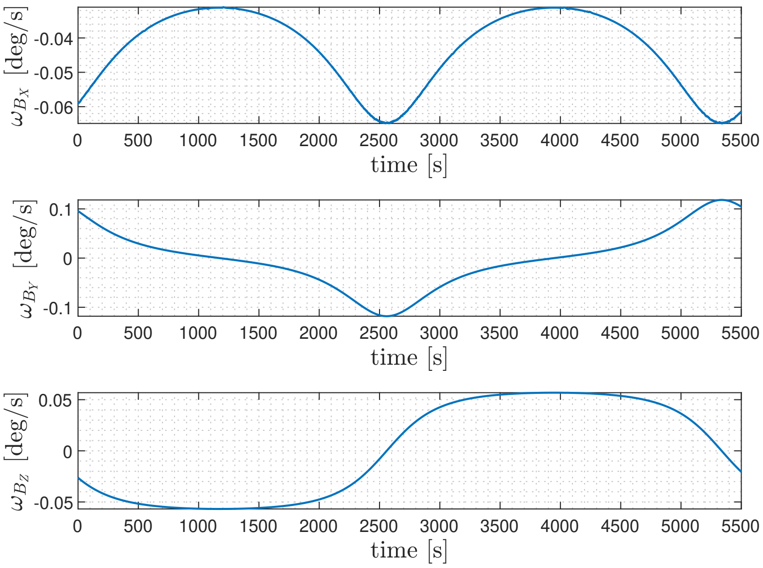

Figure 5.2. B2N true angular rates

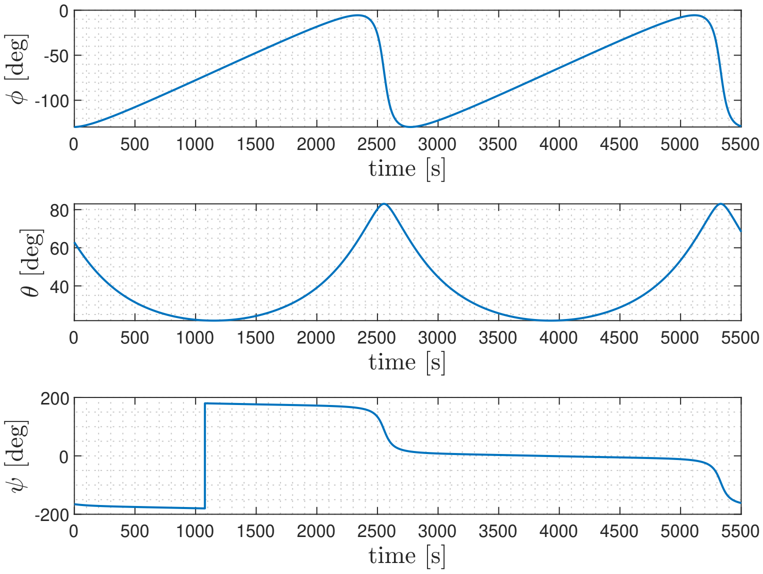

Figure 5.3. B2N true Euler's angles

The simulation compares an EKF-based observer with the SMO previously proposed (section 4.2.1). It is initially shown in figure 5.4 the error in attitude estimation wrt true state of the STR subject to misalignment. In this instance, no correction method is applied. The black line indicates SRS attitude determination error requirement (0.03°). It is clear that a misalignment profile as the one in figure 5.1 would result in unacceptable attitude estimates for the mission. For the sake of completeness, it should be noted that misalignment of STR support wrt to the nominal position is not directly visible on the 3 Euler's angles in figure 5.4 being a local error; in fact, measurements obtained from the STR are rotated from the local frame to the body reference frame and only at this point they are compared with the real ones to calculate the error.

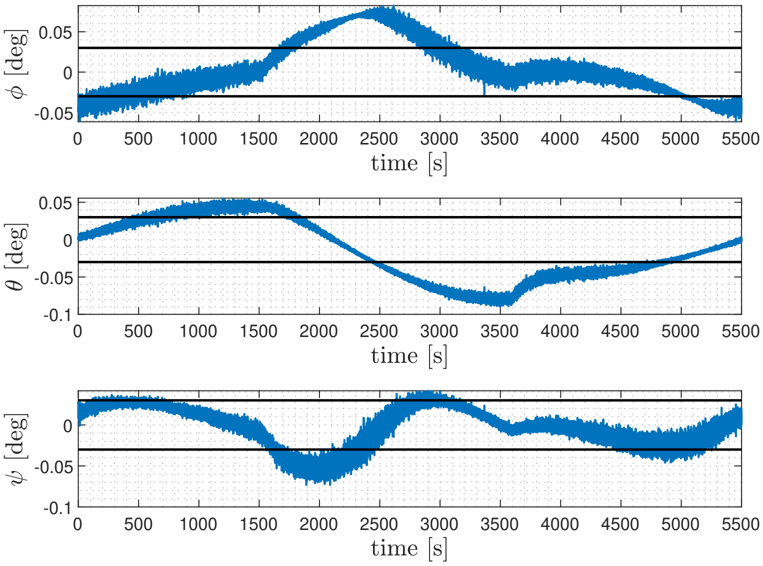

Figure 5.4. STR Attitude pointing error

Figure 5.5 finally reports the results of the applied method. It can be seen that the method correctly works with the EKF and the SMO. The main disadvantage of the use of the EKF is that it turns out to provide an attitude estimate that does not fulfil the requirement continuously along the orbit. Specifically, the points at which attitude estimation is most critical is when SRS must perform a rapid attitude change in order to guarantee the orientation of the MPCG at nadir and contemporaneously ensure sun following(figure 5.3). It is worth remembering that the errors in the STR are also a function of the spacecraft's angular rate and therefore a degradation of performance at these moments is to be expected. The main advantage of SMO is that it allows more accurate results overall. Although the inherent misalignments of the STR are still visible (bias and low-frequency errors) and are independent of the chosen observer as it should be, by using an SMO with its non-linear injection term, it is possible to obtain an estimate that significantly reduces the attitude error high-frequency oscillations.

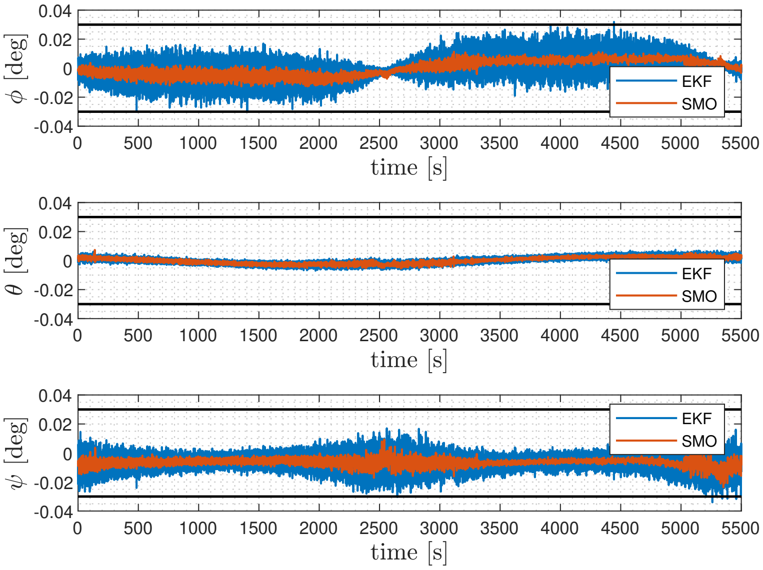

Figure 5.5. STR Attitude pointing error using the correction method

Furthermore, as can be seen in figure 5.6, the attitude error is more dependent on the variation of the spacecraft attitude along the orbit than on the magnitude of the misalignment itself. It can be said that the performance of the identification and compensation method is independent of the magnitude of misalignments but depends on the stability and precision of the observer. To demonstrate this statement, the misalignment estimation performed by SMO is compared with the imposed real one. Estimation is less accurate and stable during rapid changes in attitude, whereas during the transition between the eclipse and non-eclipse conditions (or vice versa), the algorithm suffers no loss of performance.

Additionally, figure 5.6 shows a constant bias on the estimation on each axis. This is easily explained again by the modelling of STR internal biases. Each STR has a bias on each axis, higher on the roll one than on the others (table 2.1). Due to the fact that measurements affected by errors are collected in the STR local reference frame and subsequently rotated in the body reference frame, it becomes clear that it is not straightforward to trace the error source. It seems likely that in this case the STR intrinsic limitations to measure on the roll axis are visible on the first Euler's angle.

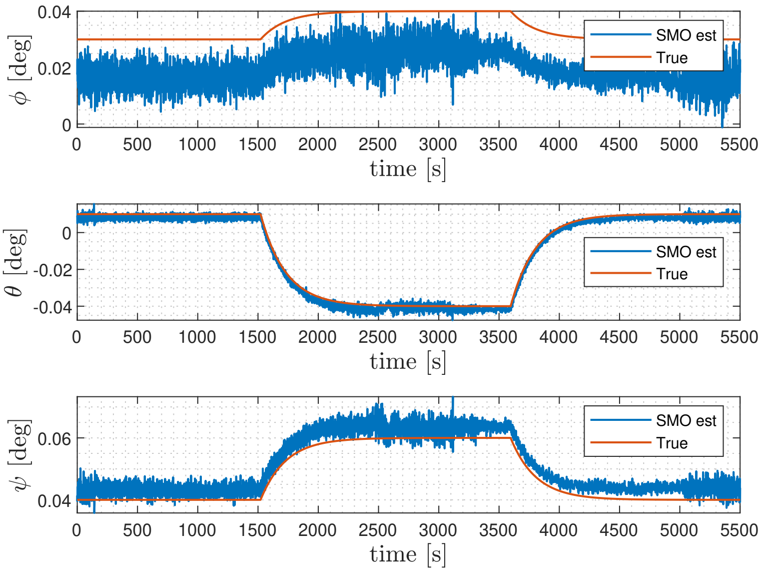

Figure 5.6. Estimation of STR misalignment using SMO

In addition, it will be useful to gather data during the first missions to characterise the magnitude of misalignment along the orbit. Due to the fact that the mission will have a limited duration and the orbit will be kept constant, it can be assumed that given a certain attitude profile, the intensity of such misalignment is repeatable along orbits. Therefore, it is imperative to characterise them and consider their impact on the GNC subsystem.

5.2 Reaction Wheel off-nominal behaviours

In this section, algorithms proposed for RW off-nominal behaviours are applied to simulations of real operating conditions of the SRS. Before presenting the results, the setting and purposes of the simulations are explained hereafter.

Deeping the explanation of sub-section 3.3.2, for the aim of this work we define a degraded behaviour of a RW as an operating condition with an efficiency which differs from the unity. Due to real effects that deviate behaviour from ideality, it can be considered a degraded functioning a RW whit an efficiency lower than 80/90%, since higher values fall indeed within the scattering range of the actuator.

The loss of efficiency of the actuator is simulated by including a decrease in torque output in the actuator model. The decrease occurs for two causes, which aim to reproduce real effects:

1. A constant loss of efficiency, reproducing any problems with electronics, lubrication deficiencies and problems involving slow changes over time. As a first approximation, these effects can be considered constant along the orbit, but faster variations will also be analysed in the simulations to verify the robustness of the algorithm.
2. A variable loss of efficiency which depends on the rotational speed of the RW. This effect simulates high-speed wheel dynamics, including problems related to lubrication or side effects which might arise over a certain speed.

A second consideration must be made about the simulated operating condition. The B2N attitude keeping is again simulated, as it is the mode that will be used mainly during science operations together with its mirror B2Z, and for this reason, it is of paramount importance to demonstrate high performance even under degraded actuation. If previous analyses were performed on a specific date, it is now necessary to distinguish different cases. It must be remembered that during B2N, to guarantee a perfect Sun following, SRS have to perform oscillations around the Nadir direction (figure 3.1). This attitude oscillation is more rapid and thus demanding for actuators when β[1] angle decrease. This is why there is the aforementioned economic Sun following, but for an optimal solar array exposure, it is advisable to keep the nominal mode as long as possible. Analyses are therefore carried out for different β angles, and results will be assessed on the basis not only of the attitude control errors but also on the operative conditions faced by RWs, in terms of actuated torque and saturation. The orbit is once again circular, with a height of $400km$ and is inclined of 7°. For the sake of completeness, considering a RAAN of 205°, it turns out that simulations performed for January the 1st 2025 have a very high and therefore favourable β angle, while the most difficult situation occurs on March the 27th when β hits the zero value.

---

[1] β is the angle between the satellite's orbital plane and the geocentric position of the Sun

Furthermore, whereas in the study of STR misalignments it was taken into account the determination error requirement, here it is considered the control error one, which is 0.04°, as reported before. Lastly, since the intention is not to verify the controller performance but to test the identification and compensation method, the initial transient part of simulations will not be discussed; it is in fact sufficient to know that the controller succeeds in bringing the states to the desired state within the desired finite timing.

5.2.1 Case 1: Single Off-Nominal RW

In this first simulation, a 50% efficiency is set on the second RW, and in addition, the efficiency of each RW is reduced by 15% when the rotational speed exceeds $3000 rpm$. The simulations are performed on 5 orbits, which correspond to approximately 8 hours of operations. The true states are the same as those shown in figures 5.2 and 5.3, to be projected for five orbits.

The first simulation reproduces a condition where $\beta = 29.7°$, which is one of the most favourable conditions. Three simulations are shown in the graphs: one is performed on the system which is under a nominal functioning (*Nominal*), the second on the system whose RW has a degraded behaviour but without correction algorithm (*Off-nominal*), and the last one uses a system where the RW has again a degraded behaviour, but to which correction algorithms are applied (*Off-nominal corrected*).

Figure 5.7 shows attitude errors, and also indicates in black the attitude error requirement. It can be clearly seen that the applied method provides much more accurate results, in which the resulting errors are of the same order of magnitude as in the nominal simulation, i.e. the controller error. In this case, given the high β angle, even in the off-nominal case without correction, the attitude error still stays within the requirements.

Figure 5.8 shows on the other hand the angular rate error. Again, the resulting smaller overall error can be appreciated on each axis when the compensation method is applied.

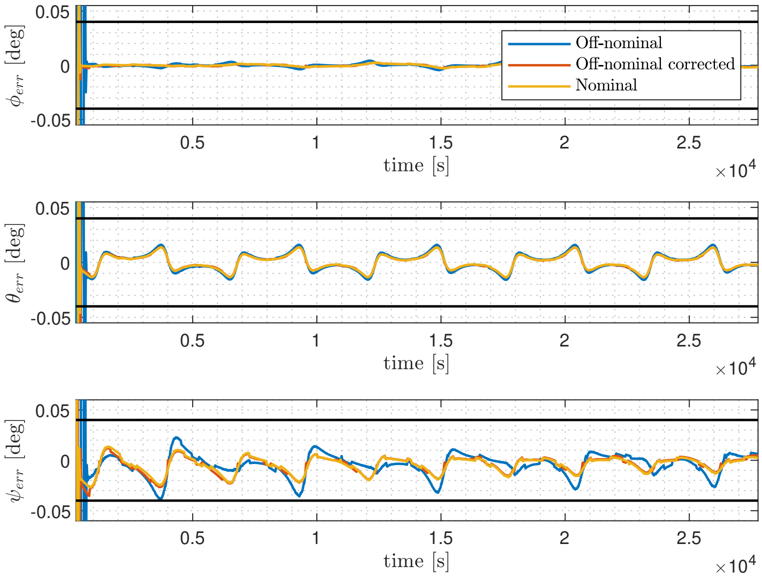

Figure 5.7. Case 1: Attitude error ($\beta = 29.7°$)

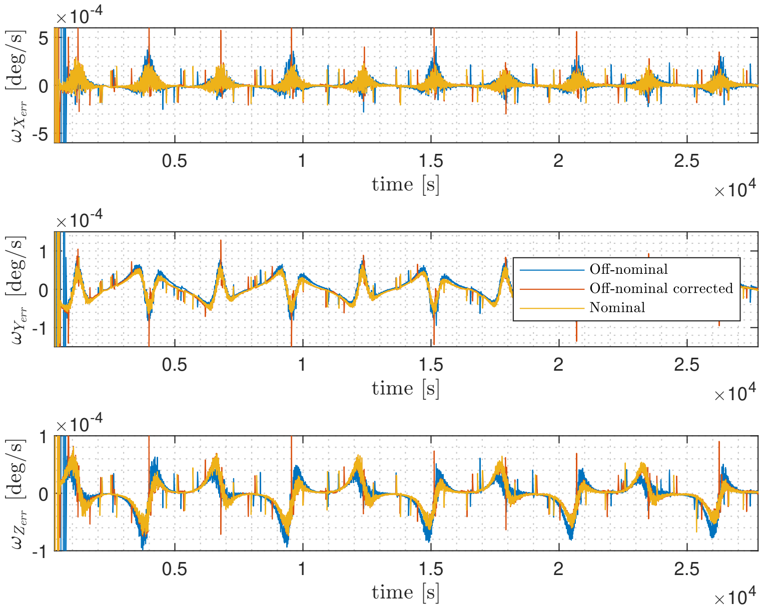

Figure 5.8. Case 1: Angular rate error ($\beta = 29.7°$)

Another significant plot to be reported is the angular momentum of each RW (figure 5.9). In contrast to previous trends, there is not much difference between cases. This can be easily explained by the fact that the controller, being a proportional-derivative one, takes the attitude and angular rate errors to calculate the torque to be provided. Because of the higher errors, in the off-nominal non-corrected case the commanded torque is higher, but due to the off-nominal RWs functioning the overall effect on the angular momentum is similar to the corrected case, i.e. the actuated torque is similar.

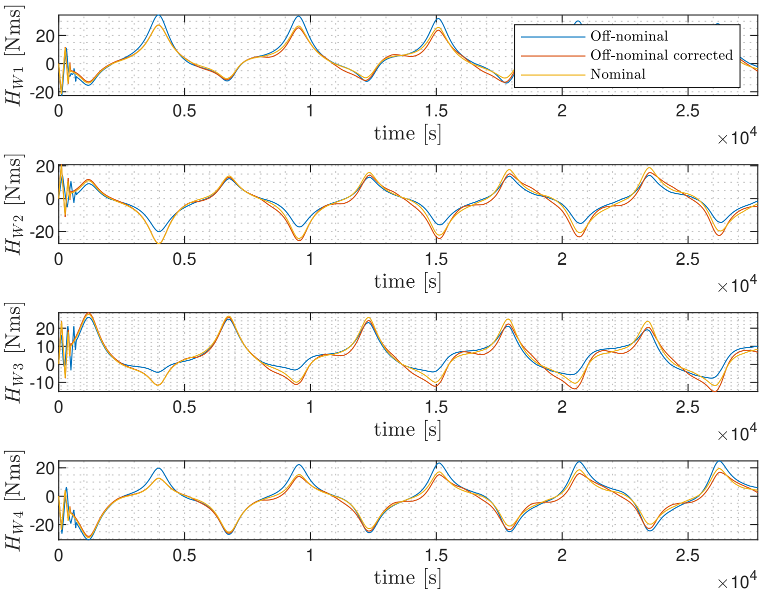

Figure 5.9. Case 1: RWs Angular Momentum ($\beta = 29.7°$)

In conclusion, as might be expected, in this attitude keeping under conditions where the demand on the actuators is limited, the proposed method improves performance, but a lack of it would not jeopardise the success of the mission: the controller would be able to keep errors within an acceptable range.

Moving towards a more demanding condition from the actuation point of view, a B2N with $\beta = 16.8°$ is now considered. Figure 5.10 shows how in this new condition, the application of the identification and compensation method is crucial in order to fulfil the attitude error requirement. It can be seen that by having faster attitude changes to guarantee Sun following with higher torque required, any deficiency on a wheel results in large errors. The same considerations can be made for angular velocity errors (figure 5.11), where errors increase sensibly each time SRS rotates.

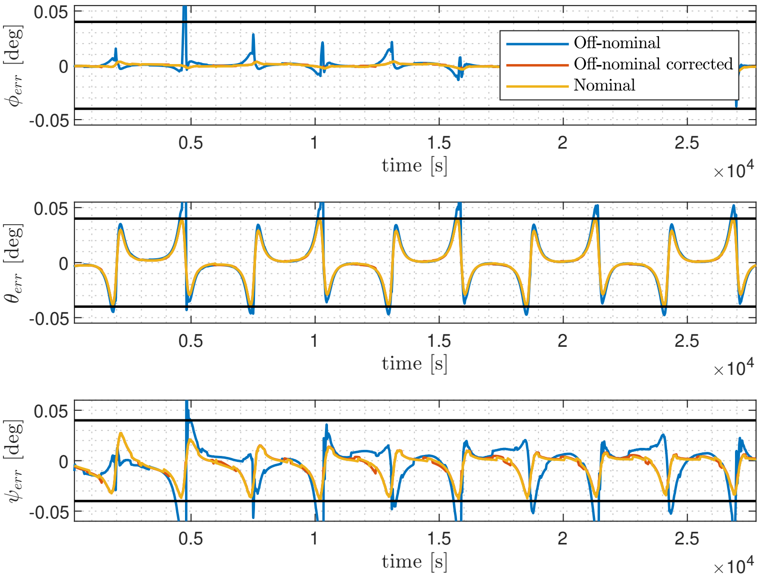

Figure 5.10. Case 1: Attitude error ($\beta = 16.8°$)

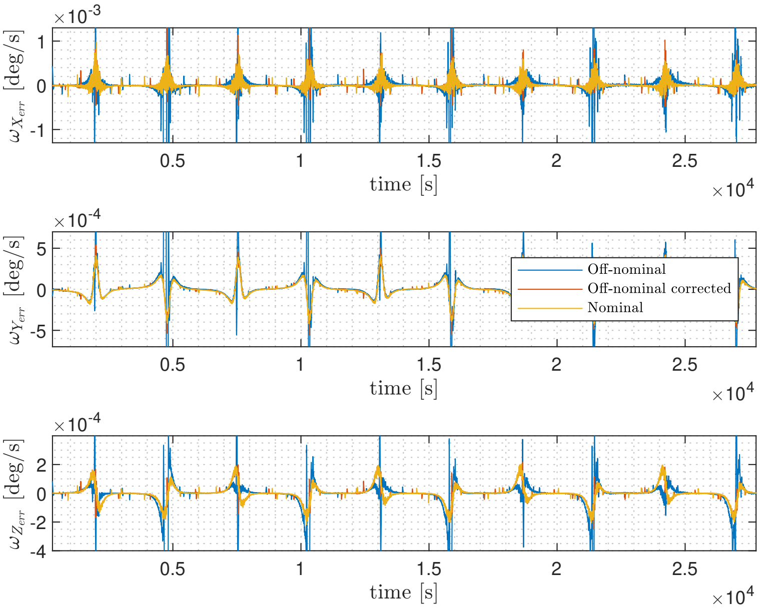

Figure 5.11. Case 1: Angular rate error ($\beta = 16.8°$)

The tendency of angular moments, in this case, would qualitatively be the same ad the one already shown in figure 5.9, for the aforementioned considerations. To further demonstrate the statements, it is interesting to observe how the actuated torque differs from the commanded one in the two off-nominal condition, i.e. with and without the applied method. Figure 5.12 shows the condition without the correction: it can be clearly seen that what changes is the commanded torque, because having higher errors will induce the controller to command higher torques, which will be decreased during actuation due to reduced efficiency. In the end this actuated torque is about the same as that actually actuated by the system with correction (figure 5.13), with the remarkable difference that in the latter case, the actuated torque is about the same as the commanded, evidence of the lower attitude and angular errors. To sum up, the torque actuated is almost equal for the two cases, and consequently the angular momentum of the wheels; what changes between the two is the resulting errors on the state variables.

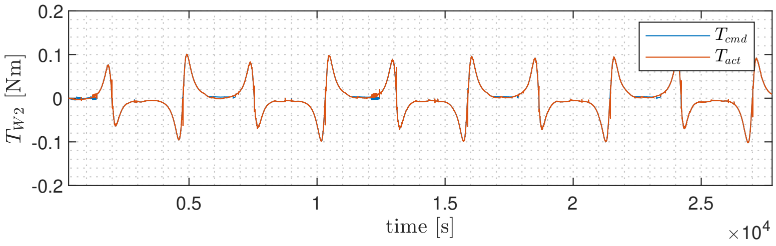

Figure 5.12. Case 1: RW2 Off-Nominal Torque ($\beta = 16.8°$)

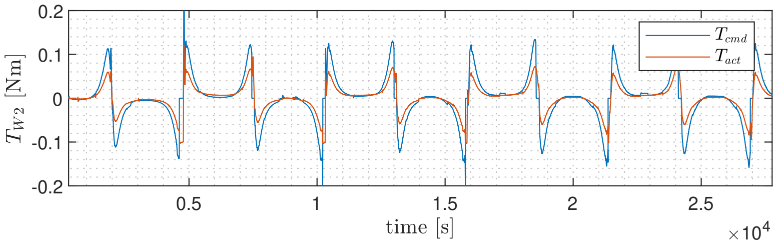

Figure 5.13. Case 1: RW2 Off-Nominal Corrected Torque ($\beta = 16.8°$)

Furthermore, an inherent limitation found in the method itself can be observed in the latter figure. By defining efficiency as $e_i = T_{act_i}/T_{est_i}$, problems may arise whenever the torque is close to zero value since approximations introduced by the simplified estimation model can cause the actuated and the estimated torque to assume different signs even if close in value. Such a situation would make the parameter e meaningless and, for this reason, when the torque is under the 10% of the maximum value, the efficiency parameter is kept fixed and the calculation is not pursued. The second critical point in the proposed method is when the angular momentum crosses the zero value, that is when the wheel changes rotation direction and then there are uncertainties related to the break-away friction. These can create locally large discrepancies in the estimation of the parameter e, but it is simply sufficient once again to suspend temporarily the efficiency calculation. The visible effect of these two suspensions of the algorithm in the analysed cases is noticeable both in figure 5.13, where torque has occasionally small discontinuities, and in the calculation of state errors, where in some instants some spurious peaks are observable, associated precisely to the formulation and not to real state errors.

By reducing further the β angle, it would no longer be possible to stay within the requirements, even with the nominal functioning. Figure 5.10 makes it clear that the second Euler's angle is reaching the imposed boundary under these conditions. It would be necessary to accept a larger error or to switch to the economical sun following, which at the cost of having a less optimal lighting condition, requires less effort to the actuation system.

5.2.2 Case 2: Multiple Off-Nominal RWs

The procedure proposed in chapter 4 is subject to certain limitations. Specifically, in order to seek an optimal redistribution of torque in the 3 body axes to the 4 RWs, it is necessary that the torque does not saturate, otherwise, the redistribution falls back into a condition where the problem becomes uniquely determined (3-axis torque to be distributed to the 3 RWs available), and the L_∞ norm optimisation is no more possible. This is not to be seen as something to be avoided, it is an inherent limitation of the actuation system used, which can be encountered whenever the required torque is high. However, to demonstrate the performance of the proposed algorithm, it is important that analysed situations are those in which RWs don't saturate in torque. This is the way to obtain objective results that are not tainted by this physical limitation.

With this consideration clearly in mind, we move on to consider a case study in which 3 RWs have suffered a loss of efficiency. Specifically, the B2N mode is again simulated, which being an attitude keeping ensures a torque supply far from saturation if compared to other manoeuvres (i.e. Slew). It can be globally expected higher state errors having several off-nominal actuators, and consequently an application of the proposed algorithm could show even greater performances.

The imposed efficiencies on actuators are the following ones:

- 1st RW: 50%
- 2nd RW: decreasing from 100% to 40% during the first 5h, constant afterwards
- 3rd RW: 100%
- 4th RW: 70%

Moreover, the efficiency of each RW is again reduced by 15% when the rotational speed exceeds $3000 rpm$.

The first presented case (figures 5.14 and 5.15) reports a condition where $\beta = 29.7°$.

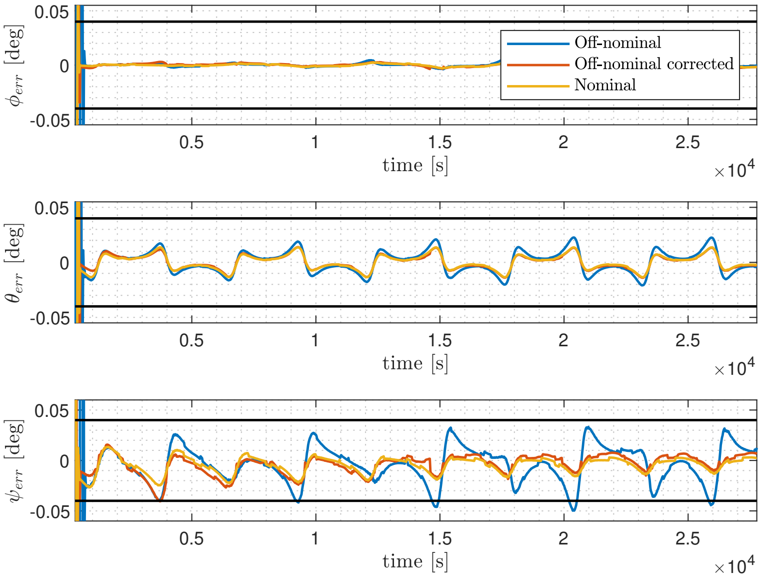

Figure 5.14. Case 2: Attitude error ($\beta = 29.7°$)

In contrast to the previous case, it can be seen here that with a larger number of off-nominal actuators, in the case without correction it would not be possible to remain within the requirements on attitude error, as shown in figure 5.14. It is also noteworthy that without applying the identification and compensation method, this error tends to increase over time and it becomes increasingly detached from the one of the corrected case .

A similar trend to the one described above can be seen on the angular rate errors, shown in figure 5.15.

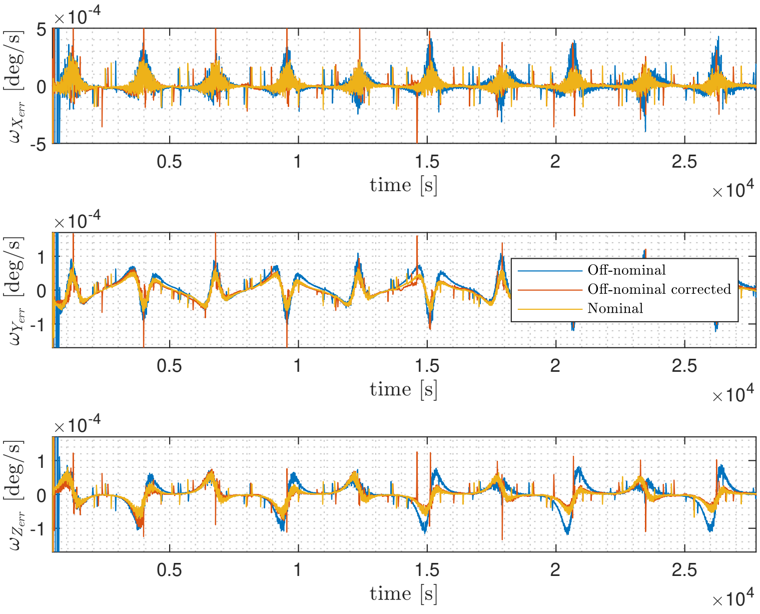

Figure 5.15. Case 2: Angular rate error ($\beta = 29.7°$)

Moving on to the case where $\beta = 16.8°$, the behaviour is again noticeable: figure 5.16 shows that errors in the uncorrected case are much higher, and the tendency is that these errors increase in amplitude as time progresses. With reduced efficiencies on multiple actuators, it is clear how the uncorrected system reallocation struggles more and more to follow the desired states having multiple causes of discrepancy; on the other hand, the system with the applied correction method shows again very promising results, managing to achieve attitude estimation errors fully comparable with the ones of the nominal case.

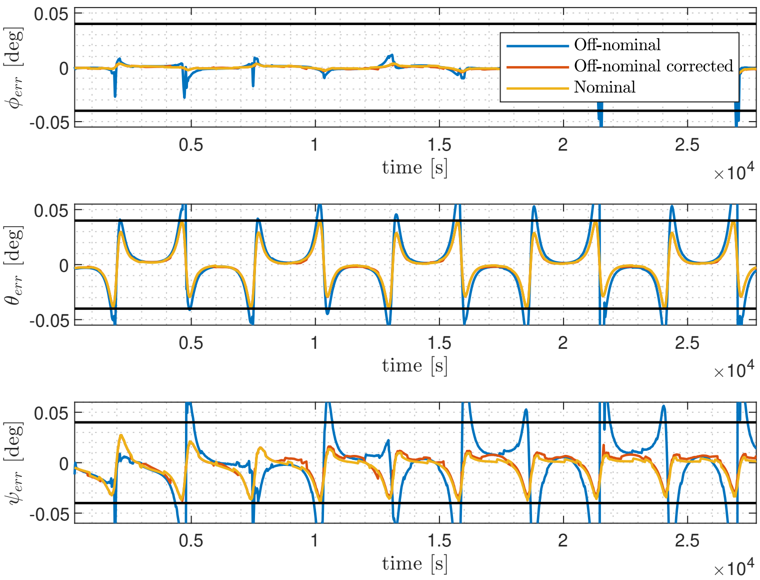

Figure 5.16. Case 2: Attitude error ($\beta = 16.8°$)

Figure 5.17 shows that the errors on the angular rates of the uncorrected system also increase significantly under these actuation conditions. But again, the compensation method demonstrates robustness wrt the variation of off-nominal conditions.

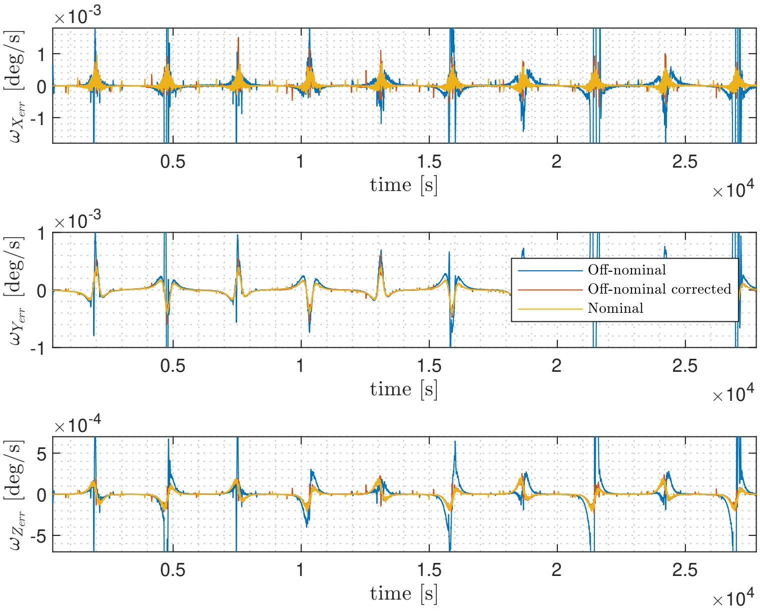

Figure 5.17. Case 2: Angular rate error ($\beta = 16.8°$)

For the sake of completeness, figure 5.18 shows the 4 RWs' angular momentums.

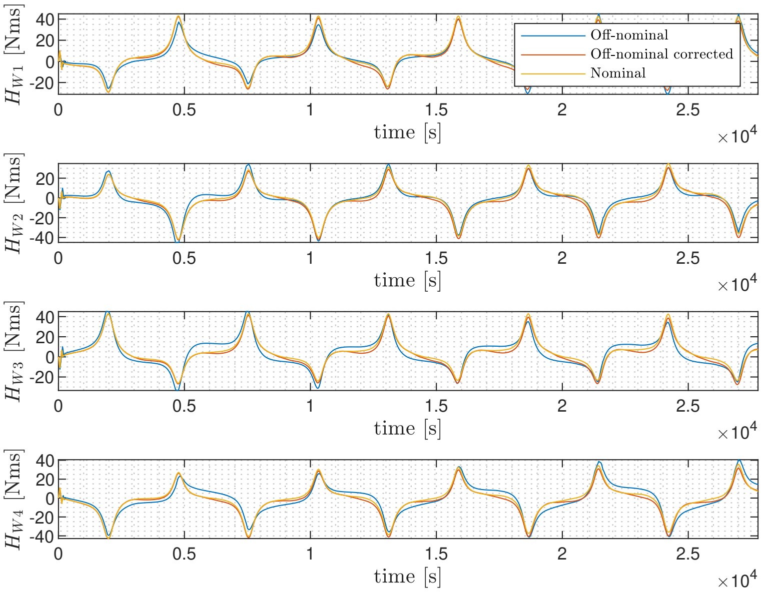

Figure 5.18. Case 2: RWs Angular Momentum ($\beta = 16.8°$)

As aforementioned, the trends of the different cases are comparable. An interesting difference is however visible in the trend of the commanded and actuated torques in the off-nominal case with and without correction. This time, multiple RWs work off-nominally and thus figures provide torque trends of each RW. Figure 5.19 shows the behaviour of the off-nominal system without correction, and as it can be seen there is a reduction in commanded torque of factors e_i. As noted earlier, a higher commanded torque means higher errors ahead. The final effect, i.e. the actuated torque, is comparable to the case in which the correction is applied (figure 5.20), where however the error wrt the desired stated is kept bounded.

Although a very similar actuated torque results by using or not the applied method, it might be thought that the method is not so useful in the end. To disprove this statement, it must be remembered that in addition to having smaller state errors, the method allows having a system without discrepancies in the actuation, a fact of fundamental importance in the life of a system in orbit. In fact, in a hostile space environment, it is important to identify any discrepancy between expected and executed behaviour. Classifying these off-nominal RW functioning allows for a greater chance of identifying any other off-nominal system behaviours, reducing then the risk of a superposition of effects that would inevitably lead to greater uncertainties.

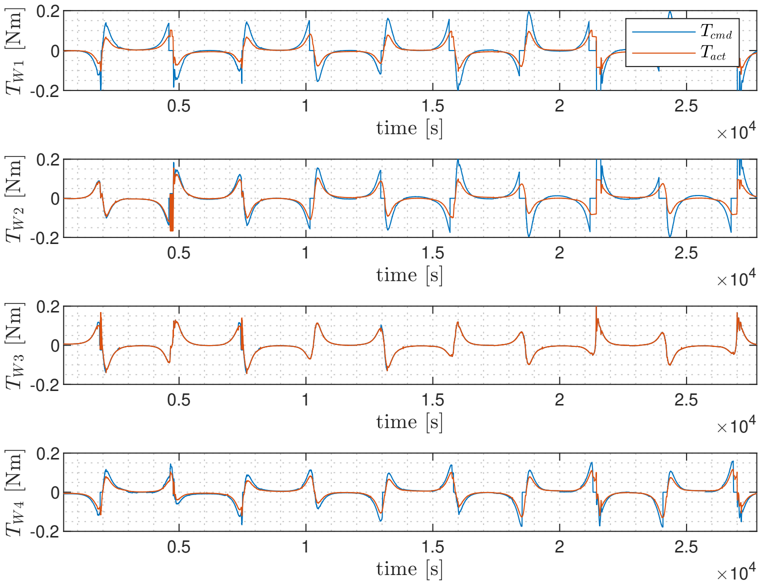

Figure 5.19. Case 2: RW Off-Nominal Torque ($\beta = 16.8°$)

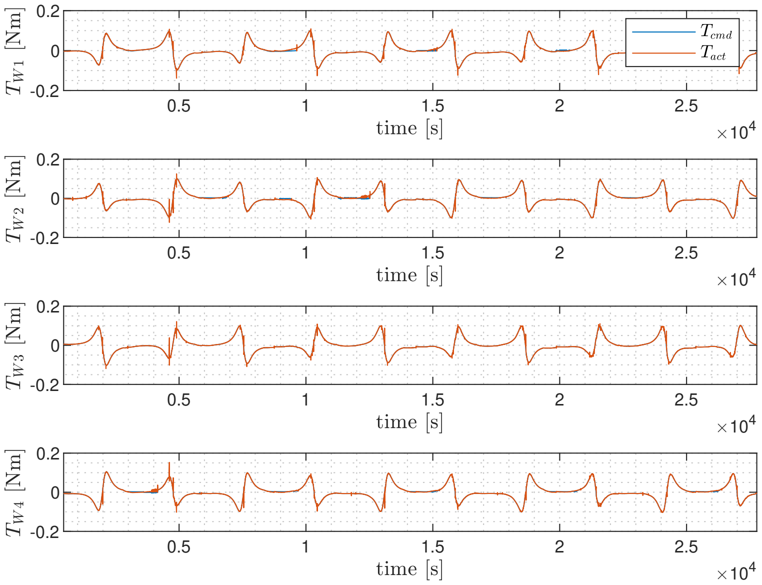

Figure 5.20. Case 2: RW Off-Nominal Corrected Torque ($\beta = 16.8°$)

5.3 Conclusions and Future Works

In conclusion, it can be stated that the applied methods allow for increased GNC performances. The two methods dealt with different problems but gave satisfactory results by using simple models and making simple considerations. Undoubtedly, however, methods present some criticalities that will be listed below, and on which further study would be necessary.

The misalignment compensation of STRs makes use of the sliding mode observer and aims to compensate for unknown potential misalignments of sensors in orbit. It is difficult to have *a priori* information on the magnitude and the variability of these misalignments, and consequently, it should be demonstrated that the observer is able to guarantee the required performance over a wide range of situations. This process could be performed with post-flight analysis after the maiden flight, using mission data to validate the method, or with more simulations to be carried out over a greater number of conditions once more data on the behaviour of the structure in orbit has been provided.

With regard to the behaviour of the RWs, the study was limited to one specific case of malfunctioning, which even though it is a consequence of multiple failure causes, it does not include all failure cases. The first action needed would be to expand the study to include more degraded cases, and integrate them all into a FTC.

Focusing now on the implemented method, it is necessary to make some remarks on the limitations encountered. First of all, as mentioned earlier, the method aims to find the optimal solution to the torque allocation problem: this objective can be pursued as long as the torque on some reaction wheel doesn't saturate, as at that point the problem is either uniquely determined (3 RWs) or under-determined (2 RWs or less). Therefore, a detailed study should be carried out on cases subject to saturation. Secondly, problems arising when torques are close to zero or when the RW's angular momentum is close to zero suggest that a more in-depth study of equivalent formulations would be necessary to provide continuity to the method also under these circumstances.

Bibliography

[1] ESA, "Space rider: Europe's first reusable space transportation system." https://www.esa.int/Space_Rider.

[2] Y. Shtessel, C. Edwards, L. Fridman, A. Levant, *et al.*, *Sliding mode control and observation*, vol. 10. Springer, 2014.

[3] A. Filippov, "Application of the theory of differential equations with discontinuous right-hand sides to non-linear problems in automatic control," *IFAC Proceedings Volumes*, vol. 1, no. 1, pp. 933–937, 1960.

[4] V. Utkin, "Variable structure systems with sliding modes," *IEEE Transactions on Automatic control*, vol. 22, no. 2, pp. 212–222, 1977.

[5] A. Levant, "Sliding order and sliding accuracy in sliding mode control," *International journal of control*, vol. 58, no. 6, pp. 1247–1263, 1993.

[6] J. Davila, L. Fridman, and A. Levant, "Second-order sliding-mode observer for mechanical systems," *IEEE transactions on automatic control*, vol. 50, no. 11, pp. 1785–1789, 2005.

[7] I. Nagesh and C. Edwards, "A multivariable super-twisting sliding mode approach," *Automatica*, vol. 50, no. 3, pp. 984–988, 2014.

[8] A. Levant, "Robust exact differentiation via sliding mode technique," *automatica*, vol. 34, no. 3, pp. 379–384, 1998.

[9] H. Alwi, C. Edwards, and C. P. Tan, *Fault detection and fault-tolerant control using sliding modes*. Springer, 2011.

[10] Q. Wu and M. Saif, "Robust fault diagnosis of a satellite system using a learning strategy and second order sliding mode observer," *IEEE Systems Journal*, vol. 4, no. 1, pp. 112–121, 2010.

[11] F. L. Markley and J. L. Crassidis, *Fundamentals of spacecraft attitude determination and control*, vol. 1286. Springer, 2014.

[12] M. D. Shuster and S. D. Oh, "Three-axis attitude determination from vector observations," *Journal of guidance and Control*, vol. 4, no. 1, pp. 70–77, 1981.

[13] G. Wahba, "A least squares estimate of satellite attitude," *SIAM review*, vol. 7, no. 3, pp. 409–409, 1965.

[14] P. B. Davenport, *A vector approach to the algebra of rotations with applications*, vol. 4696. National Aeronautics and Space Administration, 1968.

[15] J. L. Farrell, “Attitude determination by kalman filtering,” *Automatica*, vol. 6, no. 3, pp. 419–430, 1970.

[16] C. K. Chui, G. Chen, *et al.*, *Kalman filtering.* Springer, 2017.

[17] M. E. Pittelkau, “Survey of calibration algorithms for spacecraft attitude sensors and gyros,” *Adv. Astronaut. Sci.*, vol. 129, pp. 651–706, 2008.

[18] A. A. Amin and K. M. Hasan, “A review of fault tolerant control systems: advancements and applications,” *Measurement*, vol. 143, pp. 58–68, 2019.

[19] R. Martínez-Guerra and J. J. Rincón-Pasaye, “Fault estimation using sliding mode observers,” *IFAC Proceedings Volumes*, vol. 40, no. 20, pp. 649–654, 2007.

[20] C. C. De Wit and J.-J. Slotine, “Sliding observers for robot manipulators,” *Automatica*, vol. 27, no. 5, pp. 859–864, 1991.

[21] P. Baldi, M. Blanke, P. Castaldi, N. Mimmo, and S. Simani, “Adaptive ftc based on control allocation and fault accommodation for satellite reaction wheels,” in *2016 3rd Conference on Control and Fault-Tolerant Systems (SysTol)*, pp. 672–677, IEEE, 2016.

[22] ESA, “Ixv.” https://www.esa.int/IXV.

[23] ESA, “Vega-c.” https://www.esa.int/Vega-C.

[24] W. R. Hamilton, “On quaternions; or on a new system of imaginaries in algebra,” *The London, Edinburgh, and Dublin Philosophical Magazine and Journal of Science*, vol. 25, no. 163, pp. 10–13, 1844.

[25] J. R. Wertz, *Spacecraft attitude determination and control*, vol. 73. Springer Science & Business Media, 2012.

[26] K. J. Aastrom and C. Canudas-de Wit, “Revisiting the lugre model; stick-slip motion and rate dependence,” *IEEE Control Systems Magazine*, vol. 28, 2008.

[27] H. Yoon, H. H. Seo, and H.-T. Choi, “Optimal uses of reaction wheels in the pyramid configuration using a new minimum infinity-norm solution,” *Aerospace Science and Technology*, vol. 39, pp. 109–119, 2014.

[28] A. Gelb *et al.*, *Applied optimal estimation.* MIT press, 1974.

[29] M. S. Grewal and A. P. Andrews, *Kalman filtering: Theory and Practice with MATLAB.* John Wiley & Sons, 2014.

[30] J. L. Crassidis and J. L. Junkins, *Optimal estimation of dynamic systems.* Chapman and Hall/CRC, 2004.

[31] F. L. Markley, “Attitude error representations for kalman filtering,” *Journal of guidance, control, and dynamics*, vol. 26, no. 2, pp. 311–317, 2003.

[32] S. Murugesan and P. Goel, “Fault-tolerant spacecraft attitude control system,” *Sadhana*, vol. 11, no. 1, pp. 233–261, 1987.

[33] J.-J. Slotine, J. K. Hedrick, and E. A. Misawa, “On sliding observers for nonlinear systems,” *Journal of Dynamic Systems, Measurement, and Control*, vol. 109, pp. 245–252, 09 1987.

[34] H. Majid and H. Abouaïssa, “Comparative study of a super-twisting sliding mode observer and an extended kalman filter for a freeway traffic system,” *Cybernetics and Information Technologies*, vol. 15, no. 2, pp. 141–158, 2015.

[35] Leonardo, “Spacestar - star tracker architecture.”

[36] Y. Xie, Y. Lei, J. Guo, and B. Meng, *Spacecraft Dynamics and Control.* Space Science and Technologies, Springer Singapore, 2022.

[37] M. J. Sidi, *Spacecraft dynamics and control: a practical engineering approach*, vol. 7. Cambridge university press, 1997.

[38] J. Diebel, “Representing attitude: Euler angles, unit quaternions, and rotation vectors,” *Matrix*, vol. 58, no. 15-16, pp. 1–35, 2006.

[39] D. Bonetti, G. De Zaiacomo, G. B. Arnao, G. Medici, I. P. Fuentes, and B. Parreira, “Space rider mission engineering,” in *8th European Conference for Aeronautics and Space Sciences (EUCASS)*, 2019.

[40] M. E. Pittelkau, “Autonomous on-board calibration of attitude sensors and gyros,” in *20th International Symposium on Space Flight Dynamics*, 2007.

[41] S. Gallucci, R. Mancini, E. Scardecchia, and F. Spaziani, “The avum orbital module for the space rider system,” in *8th European Conference for Aeronautics and Space Sciences (EUCASS)*, 2019.